High-order-harmonic generation in atomic and molecular systems

Noslen Suárez,[1,*] Alexis Chacón,[1] Jose A. Pérez-Hernández,[2] Jens Biegert,[1,3] Maciej Lewenstein,[1,3] and Marcelo F. Ciappina[4]

[1]*ICFO–Institut de Ciències Fotòniques, The Barcelona Institute of Science and Technology, Av. Carl Friedrich Gauss 3, 08860 Castelldefels (Barcelona), Spain*

[2]*Centro de Láseres Pulsados (CLPU), Parque Científico, 37185 Villamayor, Salamanca, Spain*

[3]*ICREA, Pg. Lluís Companys 23, 08010 Barcelona, Spain*

[4]*Institute of Physics of the ASCR, ELI-Beamlines Project, Na Slovance 2, 182 21 Prague, Czech Republic*

(Received 18 January 2017; published 16 March 2017)

High-order-harmonic generation (HHG) results from the interaction of ultrashort laser pulses with matter. It configures an invaluable tool to produce attosecond pulses, moreover, to extract electron structural and dynamical information of the target, i.e., atoms, molecules, and solids. In this contribution, we introduce an analytical description of atomic and molecular HHG, that extends the well-established theoretical strong-field approximation (SFA). Our approach involves two innovative aspects: (i) First, the bound-continuum and rescattering matrix elements can be analytically computed for both atomic and multicenter molecular systems, using a nonlocal short range model, but separable, potential. When compared with the standard models, these analytical derivations make possible to directly examine how the HHG spectra depend on the driven media and laser-pulse features. Furthermore, we can turn on and off contributions having distinct physical origins or corresponding to different mechanisms. This allows us to quantify their importance in the various regions of the HHG spectra. (ii) Second, as reported recently [N. Suárez *et al.*, Phys. Rev. A **94**, 043423 (2016)], the multicenter matrix elements in our theory are free from nonphysical gauge- and coordinate-system-dependent terms; this is accomplished by adapting the coordinate system to the center from which the corresponding time-dependent wave function originates. Our SFA results are contrasted, when possible, with the direct numerical integration of the time-dependent Schrödinger equation in reduced and full dimensionality. Very good agreement is found for single and multielectronic atomic systems, modeled under the single active electron approximation, and for simple diatomic molecular systems. Interference features, ubiquitously present in every strong-field phenomenon involving a multicenter target, are also captured by our model.

DOI: 10.1103/PhysRevA.95.033415

I. INTRODUCTION

High-order-harmonic generation (HHG) is a conversion process resulting from the extremely high nonlinear interaction of a short and intense laser pulse with gas atoms or molecules or, recently, solid targets and nanostructures [1–6]. Nowadays, the HHG process is the conventional route for the production of spatially and temporally coherent extreme-ultraviolet (XUV) light, as well as light pulses in the subfemtosecond and attosecond regimes [7]. Coherent light sources in the ultraviolet (UV) to XUV spectral range are ubiquitously employed in a broad range of subjects, including basic research, material science, biology, and lithography [3]. Furthermore, the molecular HHG process encodes electronic orbital structure information and presents, as a consequence, a reliable method to retrieve molecular intrinsic parameters with attosecond and sub-Ångström temporal and spatial resolution, respectively [8–12]. Taking this objective in mind, a large amount of both theoretical and experimental work have been conducted in order to optimize, improve, and understand the molecular HHG process. Furthermore, HHG in atoms is one of the most studied topics of strong-field physics and several theoretical models, aside from the solution of the time-dependent Schrödinger equation (TDSE), have been developed to describe it. Amongst them, the most successful and widely used is the strong-field approximation (SFA) [13,14].

The underlying physics of the HHG process is usually understood by invoking the so-called "three-step model": (i) tunnel ionization, (ii) propagation in the laser field "continuum," and (iii) recombination with the parent ion [14,15]. According to this approach, when a strong laser pulse interacts with an atomic or molecular target, a bounded electron is liberated through tunnel ionization (this happens when the laser electric field is close to its peak during an optical cycle). This "free" electron is then driven away from the ionic core and accelerated by the laser electric field, developing an oscillating trajectory. During this journey, the electron accumulates kinetic energy, that is released during the recombination process in the form of a high-energy photon. As this three-step process usually occurs every half-cycle of the laser field, the spectrum of the generated coherent radiation consists of peaks at odd integer multiples of the driven laser frequency.

On the other hand, for multicenter molecules, much less experimental [2,16–21] and theoretical [18,22–30] work have been done. The direct numerical solution of the TDSE for more complex systems, with more than two centers, is a quite challenging and formidable task from the numerical and computational viewpoints. Even for the simplest diatomic molecule, one has to solve a three-dimensional TDSE (3D-TDSE), that typically requires the utilization of a multicore CPU and large amount of memory. In addition, the interpretation of the results extracted from the TDSE is a not trivial subject, in particular if one wants to disentangle the underlying physical mechanisms contributing to the total HHG spectrum.

*noslen.suarez@icfo.es

As was mentioned above, the initial interest in the molecular HHG relies on the fact that it offers additional degrees of freedom and promising possibilities, such as the alignment of the molecular axis with respect to the laser field polarization. Specifically, for a diatomic system, the existence of a distinctive quantum-interference minima pattern in the spectra and its dependence with the molecular orientation have been theoretically predicted by Lein *et al.* [9,31,32]. It is demonstrated that this pattern is due to a destructive interference from the high-harmonic emission at spatially separated centers and the internuclear distance can be accurately obtained scrutinizing the HHG spectra. In addition, the chance of controlling the phases and improving the phase-matching condition opens a route to the investigation of this area. More importantly, research on this field revealed how the distinctive features of the molecular HHG spectra can be used to retrieve structural information in simple molecules [33]. Furthermore, the so-called HHG spectroscopy has shown the possibility to extract structural and dynamical information from the molecular HHG spectra in more complex targets (for a couple of examples see, e.g., [34–36]). Finally, studies in small molecules have demonstrated that the temporal evolution of the electronic wave function can be directly recovered [37–39].

In this paper, we use the SFA within the framework of the Lewenstein's model to study HHG both from atoms and two- and three-center molecular systems in the few-cycle infrared (IR) laser-pulse regime. The derivation for the molecular systems is constructed as a consecutive extension of the atomic model. For simplicity, our analytical model is based on a nonlocal potential which has approximately a short-range (SR) character. We compute HHG spectra for those three systems and, for the atomic case, compare the results with the numerical solution of the 3D-TDSE in the single-active-electron (SAE) approximation.

Our approach involves two innovative aspects: (i) First, using a model nonlocal, but separable, potential we analytically calculate the bound-free dipole and the rescattering transition matrix elements for both the atomic and molecular multicenter systems. In comparison with the standard approaches to the HHG process, this analytic derivation of the different matrix elements gives us the possibility to study directly how the HHG spectra depend on the atomic target and laser-pulse features; we can turn on and off contributions having distinct physical origins or corresponding to different physical mechanisms. This allows us to quantify their weights in the various regions of the HHG spectra. (ii) Second, as in Ref. [40], in our theory the dipole matrix elements are free from nonphysical gauge- and coordinate-system-dependent terms; this is achieved by adapting the coordinate system, in which SFA is performed, to the center from which the corresponding part of the time-dependent wave function originates. We compare, when possible, our SFA results with the numerical solutions of the TDSE in full dimensionality. Excellent agreement is found for atomic and molecular systems, including multielectronic systems modeled under the SAE. Our model captures also the interference features, ubiquitously present in any multicenter target.

This article is organized as follows. In Sec. II, we address the main theory describing the HHG process and, in particular, the derivation of the time-dependent dipole matrix element within the SFA. Here, we make use of the results previously presented in [40,41] to obtain the analytical expressions needed to compute each of the individual contributions. Particularly for the three-center molecular system, we develop a new set of equations to compute the time-dependent dipole matrix element, making use of the nonlocal SR potential bound states. In Sec. III, HHG spectra for the atomic and molecular cases are numerically calculated. Results in hydrogen and argon atoms are presented, comparing them with those obtained from the 3D-TDSE. For diatomics, we analyze two systems: $H_2{}^+$ and H_2. For the $H_2{}^+$ case, the basic analysis of the interference minima of the HHG spectra with respect to the molecular orientation is discussed. In addition, the contribution of the different processes to the total harmonic radiation is assessed. A time analysis of the HHG spectra using a Gabor transformation is performed and the influence of the short and long trajectories is investigated. In addition, CO_2 and H_2O define our three-center molecular systems. For both cases, we investigate the dependence of the HHG spectra with respect to the molecular orientation and extract information about the different mechanisms contributing to the total HHG spectra. Finally, in Sec. IV, we summarize the main ideas and present our conclusions. Atomic units will be used throughout the paper unless otherwise stated.

II. THEORY OF HHG WITHIN THE SFA

In this section, we develop a quantum mechanical approach of HHG using the generalized SFA model described in Refs. [13,14]. The source of the additional frequencies that are generated during the interaction of a strong laser pulse with an atomic or molecular target is the nonlinear dipole oscillation of the medium. Therefore, the aim is to calculate this dipole response by means of the solution of the TDSE. The time-dependent dipole moment reads as

$$\vec{\mu}(t) = -\langle \Psi(t)|\mathbf{r}|\Psi(t)\rangle, \tag{1}$$

where $|\Psi(t)\rangle$ is the state describing the time evolution of the atomic or molecular system under study. In general, within the SFA statement, we can write the wave function of the whole system as a superposition of the ground $|0\rangle$ and continuum states $|\mathbf{v}\rangle$ as $|\Psi(t)\rangle = e^{iI_p t}[a(t)|0\rangle + \int d^3\mathbf{v}\, b(\mathbf{v},t)|\mathbf{v}\rangle]$, where the transition amplitude of the continuum states is denoted by $b(\mathbf{v},t)$. After some algebra with the above equations and only considering transitions from the bound to the continuum states, the time-dependent dipole moment reads as

$$\vec{\mu}(t) = \int d^3\mathbf{v}\, b(\mathbf{v},t)\, \mathbf{d}^*(\mathbf{v}) + \text{c.c.}, \tag{2}$$

where the bound-continuum transition dipole matrix element is defined as $\mathbf{d}(\mathbf{v}) = -\langle \mathbf{v}|\mathbf{r}|0\rangle$. The radiation emitted by a single atom is proportional to the time-dependent dipole moment $\vec{\mu}(t)$. In this way, the harmonic spectrum $I(\omega)$ is calculated as the modulus squared of the Fourier-transformed dipole acceleration $\mathbf{a}(t)$ related to the defined time-dependent dipole matrix element [Eq. (2)] by the Ehrenfest theorem as $|\tilde{\mathbf{a}}(\omega)| = |\omega^2\, \tilde{\mu}(\omega)|$. Finally, we can compute the harmonic

spectra as

$$I_{x\mathrm{N}}(\omega) \propto \left| \int_{-\infty}^{\infty} dt\, e^{i\omega t}\, \vec{\mu}_{x\mathrm{N}}(t) \right|^2. \tag{3}$$

Here, the subscript x will take the values $1,2,\ldots,n$, where n is the total number of atoms of the molecule. For case of a diatomic molecule, i.e., constituted by two atoms, the subscript is set to $x = 2$, meaning $\vec{\mu}_{2\mathrm{N}}(t)$ and $I_{2\mathrm{N}}(\omega)$. Notice that both the atomic and molecular harmonic spectra depend directly on the time-dependent dipole moment. The latter in turn depends on the form of the bound-continuum matrix element and the continuum states transition amplitude, that are different for each of atomic, diatomic, or multiatomic system under study.

A. Calculation of the time-dependent dipole moment for atomic systems: $\vec{\mu}_{1\mathrm{N}}(t)$

In order to have all the ingredients to compute the harmonic spectrum for an atomic system $I_{1N}(\omega)$, using Eqs. (2) and (3), we need to know the exact dependency of the bound-continuum matrix element and the transition amplitude for the continuum states. The method to find these quantities for an atom under the influence of an intense laser pulse has been described in our previous work [41]. We therefore take advantage of those results and only explain here the new derivations needed to tackle the HHG problem.

The transition amplitude for the continuum states of the atomic system reads as

$$b(\mathbf{p},t) = i \int_0^t dt'\, \mathbf{E}(t') \cdot \mathbf{d}[\mathbf{p} + \mathbf{A}(t')] e^{-i\, S(\mathbf{p},t,t')}, \tag{4}$$

where the exponent phase factor is "the semiclassical action" $S(\mathbf{p},t,t') = \int_{t'}^{t} d\tilde{t}\{[\mathbf{p} + \mathbf{A}(\tilde{t})]^2/2 + I_p\}$ defining all the possible electron trajectories from the "birth" time t' until the "recombination" one t.

The explicit expression for the bound-continuum matrix element obtained in [41] is

$$\mathbf{d}_{1\mathrm{N}}(\mathbf{p}_0) = i\, \mathbf{p}_0\, \frac{\left(p_0^2 + \Gamma^2\right) + \left(\frac{p_0^2}{2} + I_p\right)}{\left(p_0^2 + \Gamma^2\right)^{\frac{3}{2}} \left(\frac{p_0^2}{2} + I_p\right)^2} \left[\frac{\Gamma + \sqrt{2I_p}}{2\pi\, (2I_p)^{-1/4}} \right]. \tag{5}$$

Inserting Eqs. (4) and (5) in the time-dependent dipole moment (2), and changing variables to the canonical momentum defined by $\mathbf{p} = \mathbf{v} - \mathbf{A}(t)$, we get

$$\vec{\mu}_{1\mathrm{N}}(t) = i \int_0^t dt' \int d^3\mathbf{p}\, \mathbf{E}(t') \cdot \mathbf{d}_{1\mathrm{N}}[\mathbf{p} + \mathbf{A}(t')] \times e^{-i\, S(\mathbf{p},t,t')}\, \mathbf{d}^*_{1\mathrm{N}}[\mathbf{p} + \mathbf{A}(t)] + \mathrm{c.c.} \tag{6}$$

Equation (6) has to be understood as follows: the electron is ionized at time t' with a certain probability defined by $\mathbf{E}(t') \cdot \mathbf{d}_{1\mathrm{N}}[\mathbf{p} + \mathbf{A}(t')]$. During its excursion in the continuum the electronic wave function is then propagated until the time t, acquiring a classical phase $S(\mathbf{p},t,t')$, to finally recombine with the ion core at time t with a rate given by $\mathbf{d}^*_{1\mathrm{N}}[\mathbf{p} + \mathbf{A}(t)]$. All possible combinations of birth time and momenta must be considered and therefore a multidimensional integration is required, where their contributions are added up coherently. Note that Eq. (6) configures a highly oscillatory integral, both in the momentum $\mathbf{p}$ and t' variables. As a consequence, it is convenient to rewrite the integral over $\mathbf{p}$ using the stationary-phase approximation or saddle-point method. In order to do that, it is necessary to find the extremal points over the exponential phase. The extrema $\mathbf{p} = \mathbf{p}_s$ are found from the solutions of $\nabla_{\mathbf{p}} S(\mathbf{p})|_{\mathbf{p}_s} = \mathbf{0}$. These saddle-point momenta $\mathbf{p}_s$ thus can be written as $\mathbf{p}_s = -\frac{1}{\tau}\int_{t'}^{t} \mathbf{A}(\tilde{t}) d\tilde{t}$. Here, $\tau = t - t'$ denotes the excursion time of the electron in the continuum. Expanding the function $S(\mathbf{p},t,t')$ in a Taylor series around the roots $\mathbf{p}_s$ and then applying the standard saddle-point method to the momentum integral over $\mathbf{p}$, the time-dependent dipole moment for the atomic system results:

$$\vec{\mu}_{1\mathrm{N}}(t) = i \int_0^t dt' \left(\frac{\pi}{\varepsilon + \frac{i(t-t')}{2}} \right)^{\frac{3}{2}} \mathbf{E}(t') \cdot \mathbf{d}_{1\mathrm{N}}[\mathbf{p}_s + \mathbf{A}(t')] \times e^{-i\, S(\mathbf{p}_s,t,t')}\, \mathbf{d}^*_{1\mathrm{N}}[\mathbf{p}_s + \mathbf{A}(t)] + \mathrm{c.c.}, \tag{7}$$

where we have introduced an infinitesimal parameter ε to avoid the divergence at $t = t'$ (for a detailed discussion, see [40,41]). The harmonic spectrum $I_{1\mathrm{N}}(\omega)$ is then numerically computed inserting Eq. (7) in Eq. (3).

B. Calculation of the time-dependent dipole moment for diatomic molecular systems: $\vec{\mu}_{2\mathrm{N}}(t)$

In order to calculate the harmonic spectrum generated by a diatomic molecule, we use the results obtained in Ref. [40]. As we can extract from that reference, the general wave function describing the state for a diatomic molecule can be written as

$$|\Psi(t)\rangle = e^{iI_p t} \left[a(t)|0\rangle + \sum_{j=1}^{2} \int d^3\mathbf{v}\, b_j(\mathbf{v},t)|\mathbf{v}\rangle \right], \tag{8}$$

from which the molecular time-dependent dipole moment $\vec{\mu}_{2\mathrm{N}}(t)$ is easily obtained and has the following form:

$$\vec{\mu}_{2\mathrm{N}}(t) = \sum_{j=1}^{2} \int d^3\mathbf{v}\, \mathbf{d}^*_{2\mathrm{N}}(\mathbf{v}) b_j(\mathbf{v},t) + \mathrm{c.c.} \tag{9}$$

In the above equation, we require to insert the explicit expression for the continuum states transition amplitude $b(\mathbf{p},t)$:

$$\begin{aligned} b(\mathbf{p},t) &= b_{0,1}(\mathbf{p},t) + b_{0,2}(\mathbf{p},t) \\ &= i \sum_{j=1}^{2} \int_0^t dt'\, \mathbf{E}(t') \cdot \mathbf{d}_j[\mathbf{p} + \mathbf{A}(t')] \\ &\quad \times e^{-i\{S(\mathbf{p},t,t') + \mathbf{R}_j \cdot [\mathbf{A}(t) - \mathbf{A}(t')]\}} \end{aligned} \tag{10}$$

and the bound-continuum matrix element $\mathbf{d}_j(\mathbf{v})$.

In the derivation of the length-gauge flavor of the SFA for HHG in diatomic molecules, and in particular for the computation of the bound-continuum matrix element $\mathbf{d}(\mathbf{v}) = -\langle \mathbf{v}|\mathbf{r}|0\rangle$, an unphysical term is neglected, without giving a consistent reason or argument (see [42–44] for more details). This term, that is a linear function of the internuclear distance $\mathbf{R}$, immediately introduces convergence problems as $\mathbf{R} \to \infty$. Clearly, this behavior enters in conflict between the length and velocity gauge predictions. This controversy is observed in the case of above-threshold ionization (ATI) as well.

The root of the problem relies in the degree of approximation to handle the continuum states, considered as a set of plane waves for the molecular system, without considering the relative position of each atomic core. This creates an unphysical treatment and therefore the appearance of such undesired term. In our approach, we solve this issue by computing $\mathbf{d}_j(\mathbf{v}) = -\langle \mathbf{v}|(\hat{\mathbf{r}} - \mathbf{R}_j)|0_j\rangle$, where the bound-continuum matrix element is calculated with respect to each atomic center located at $\mathbf{R}_j$. Note that if no approximations are done, i.e., if we consider the case where $\langle \mathbf{v}|$ is a scattering wave of the field-free Hamiltonian H_0, the above-mentioned problem will not arise: the scattering waves are orthonormal to the ground states $|0_j\rangle$. However, as the main core of the SFA is to handle the continuum states as Volkov states, i.e., neglecting the influence of the residual molecular potential once the electron is in the continuum, the convergence problems would remain if we do not correct the bound-continuum matrix element. The full derivation of the bound-continuum matrix element for the ATI problem in a two-center molecular system was introduced in Ref. [40]; this bound-continuum matrix element is the same used for HHG. In addition, an extended derivation for a three-center molecular system is presented in the Appendix of this contribution.

The bound-continuum matrix element is defined by $\mathbf{d}_{2\mathrm{N}}(\mathbf{p}_0) = \sum_j^2 \mathbf{d}_j(\mathbf{p}_0)$, where $\mathbf{d}_j(\mathbf{p}_0)$ denotes the bound-continuum matrix element related to the nucleus located at the position $\mathbf{R}_j$ and is given by

$$\mathbf{d}_j(\mathbf{p}_0) = 2i\,\mathcal{M}\frac{\mathbf{p}_0\left(3p_0^2 + 2I_p + 2\Gamma^2\right)}{\left(p_0^2 + \Gamma^2\right)^{\frac{3}{2}}\left(p_0^2 + 2I_p\right)^2}\, e^{-i\mathbf{R}_j\cdot\mathbf{p}_0}. \quad (11)$$

Here, $\mathcal{M}$ is a normalization constant (for details, see Ref. [40]). Note that the index j can take the value of 1 (or 2), referring to the nucleus located at the position $\mathbf{R}_1$ on the left (or $\mathbf{R}_2$ on the right).

The time-dependent dipole moment $\vec{\mu}_{2\mathrm{N}}(t)$ thus reads as

$$\vec{\mu}_{2\mathrm{N}}(t) = i\sum_{j=1}^{2}\sum_{j'=1}^{2}\int_0^t dt' \int d^3\mathbf{p}\,\mathbf{E}(t')\cdot\mathbf{d}_j[\mathbf{p}+\mathbf{A}(t')] \times e^{-i\{S(\mathbf{p},t,t')+\mathbf{R}_j\cdot[\mathbf{A}(t)-\mathbf{A}(t')]\}}\,\mathbf{d}_{j'}^*[\mathbf{p}+\mathbf{A}(t)], \quad (12)$$

where the subscripts j and j' represent the ionization and the recombination atom positions, respectively.

Equation (12) contains information about all the recombination processes occurring in the entire molecule during the HHG phenomenon and can then be written as a sum of components as

$$\vec{\mu}_{2\mathrm{N}}(t) = \sum_{j=1}^{2}\sum_{j'=1}^{2}\vec{\mu}_{jj'}(t). \quad (13)$$

The four terms in the above equation encode all the individual molecular recombination processes. Our physical interpretation of those contributions is as follows:

(i) An electron is ionized from the atom placed at the *left* with respect to the coordinate origin at time t' with certain probability: $\mathbf{E}(t')\cdot\mathbf{d}_1[\mathbf{p}+\mathbf{A}(t')]$. During its excursion in the continuum, this electron accumulates a phase which depends on the position from where it was detached, in this case $\mathbf{R}_1$. Finally, because the electric field changes its sign and the electron returns to the vicinity of the parent ion, the probability of recombination results $\mathbf{d}_1^*[\mathbf{p}+\mathbf{A}(t)]$. In this step, the energy excess acquired from the laser electric field is converted into a high-energy photon. The whole process is then described by

$$\vec{\mu}_{11}(t) = i\int_0^t dt' \int d^3\mathbf{p}\,\mathbf{E}(t')\cdot\mathbf{d}_1[\mathbf{p}+\mathbf{A}(t')] \times e^{-i\{S(\mathbf{p},t,t')+\mathbf{R}_1\cdot[\mathbf{A}(t)-\mathbf{A}(t')]\}}\,\mathbf{d}_1^*[\mathbf{p}+\mathbf{A}(t)]. \quad (14)$$

(ii) The second term is understood in a similar way. In this case, the ionization and recombination processes occur in the core placed at the *right*. The equation describing this process, $\vec{\mu}_{22}(t)$, is similar to Eq. (14) but now considering the matrix element $\mathbf{d}_2(\mathbf{v})$: the electron is detached from and recombines at the position $\mathbf{R}_2$. The two processes described before are spatially localized (involving only one core placed at a fixed position $\mathbf{R}_1$ or $\mathbf{R}_2$) and we then refer to them as *local* processes.

(iii) The last two terms, $\vec{\mu}_{21}(t)$ and $\vec{\mu}_{12}(t)$, describe events involving two atoms at two different positions $\mathbf{R}_1$ and $\mathbf{R}_2$. Here, $\vec{\mu}_{21}$ can be understood as follows: the electron is tunnel ionized from the atom on the *right* with certain probability given by $\mathbf{E}(t')\cdot\mathbf{d}_2[\mathbf{p}+\mathbf{A}(t')]$. After this ionization event the electron starts to move under the laser electric field influence accumulating energy and acquiring a phase: $e^{-i\{S(\mathbf{p},t,t')+\mathbf{R}_2\cdot[\mathbf{A}(t)-\mathbf{A}(t')]\}}$. Finally, the electron returns back to the other core (located at the *left*) at the time t to end up its journey in a recombination process that has an amplitude proportional to $\mathbf{d}_1^*[\mathbf{p}+\mathbf{A}(t)]$. As in previous cases, the energy excess is converted and emitted in a form of a high-energy photon. Considering both centers are involved in the HHG process, we call these terms as *cross* processes. The expression describing them reads as

$$\vec{\mu}_{jj'}(t) = i\int_0^t dt' \int d^3\mathbf{p}\,\mathbf{E}(t')\cdot\mathbf{d}_j[\mathbf{p}+\mathbf{A}(t')] \times e^{-i\{S(\mathbf{p},t,t')+\mathbf{R}_j\cdot[\mathbf{A}(t)-\mathbf{A}(t')]\}}\,\mathbf{d}_{j'}^*[\mathbf{p}+\mathbf{A}(t)], \quad (15)$$

where the subscripts j and j' (now $j \neq j'$) denote the nucleus located at the *left* ($j = 1$) or *right* ($j = 2$).

Note from the above description that we have to account four different possible processes corresponding to four different time-dependent dipole moments. Two of them are *local* and the other two *cross* representing all the possible recombination scenarios in our diatomic molecule.

Similarly to the atomic case, in order to obtain the molecular time-dependent dipole moment $\vec{\mu}_{2\mathrm{N}}(t)$, we apply the saddle-point method in the momentum variable $\mathbf{p}$. In fact, the phases of the *local* contributions in Eq. (14), function on the relative positions $\mathbf{R}_{1/2}$ of the atoms, cancel each other defining a saddle-point momentum $\mathbf{p}_s$ equivalent to the one found for the atomic case (see Sec. II A). On the other hand, the *cross* processes present more complex phases, that directly depend on the position variables. For instance, in $\vec{\mu}_{21}(t)$ [$\vec{\mu}_{12}(t)$] the saddle-point momentum is described by $\mathbf{p}_{s+} = -\frac{1}{\tau}[\mathbf{R} + \int_{t'}^t \mathbf{A}(\tilde{t})\mathbf{d}\tilde{t}]\{\mathbf{p}_{s-} = -\frac{1}{\tau}[-\mathbf{R} + \int_{t'}^t \mathbf{A}(\tilde{t})\mathbf{d}\tilde{t}]\}$. In all our cases the model is employed to small internuclear distances, where the condition $R < \mathcal{E}_0/\omega^2$ is fulfilled, with $\mathcal{E}_0$ and ω_0 being the laser electric field peak amplitude and carrier frequency, respectively. As a consequence, it is not necessary to consider this saddle-point momentum definition

(for more details about the validity of this approximation, see [43]). Thus, we proceed by applying the standard saddle-point momentum to all the *local* and *cross* contributions. The total time-dependent dipole moment for our diatomic molecule then reads as

$$\vec{\mu}_{2N}(t) = i\sum_{j,j'}\int_0^t dt' \left(\frac{\pi}{\varepsilon + \frac{i(t-t')}{2}}\right)^{\frac{3}{2}} \mathbf{E}(t')\cdot\mathbf{d}_j[\mathbf{p}_s + \mathbf{A}(t')] \times e^{-i\{S(\mathbf{p}_s,t,t')+\mathbf{R}_j\cdot[\mathbf{A}(t)-\mathbf{A}(t')]\}}\,\mathbf{d}^*_{j'}[\mathbf{p}_s + \mathbf{A}(t)]. \quad (16)$$

Finally, the total HHG spectrum is calculated using Eq. (3), similarly to the atomic case, but using the time-dependent dipole moment obtained in Eq. (16). As it was discussed, four terms are needed to compute each molecular HHG spectrum. Each term represents a different process, and this is equivalent to the split made in the time-dependent dipole moment [see Eq. (13)]. We label each contribution depending on the position of the atoms, e.g., from the *left-left* term we obtain the $I_{2N,11}(\omega)$ spectrum. Similarly, we write the other three terms as $I_{2N,22}(\omega)$, $I_{2N,12}(\omega)$, and $I_{2N,21}(\omega)$, respectively.

It is convenient to identify two main contributions in the total HHG spectrum [Eq. (16)], namely, (i) ones generated for the *local* processes and (ii) others developed by the *cross* processes. In this way, we can write the total HHG spectrum as

$$I_{2N}(\omega) = I_{2N\text{-local}}(\omega) + I_{2N\text{-cross}}(\omega), \quad (17)$$

where $I_{2N\text{-local}}(\omega) = I_{2N,11}(\omega) + I_{2N,22}(\omega)$ and $I_{2N\text{-cross}}(\omega) = I_{2N,12}(\omega) + I_{2N,21}(\omega)$ denote the *local* and *cross* terms, respectively.

C. Calculation of the time-dependent dipole moment for three-center molecular systems: $\vec{\mu}_{3N}(t)$

The computation of the HHG spectrum generated by a three-center molecule using the definition in Eq. (3) involves the search of the exact bound states describing the whole system. In order to do so, we use a method similar to the one presented in Refs. [40,41]. In short, we consider a three-center molecule as a set of three atoms placed at $\mathbf{R}_1 = -\frac{\mathbf{R}}{2}$, $\mathbf{R}_2 = 0$, and $\mathbf{R}_3 = \frac{\mathbf{R}}{2}$, respectively. $\mathbf{R}$ is the so-called internuclear distance, defined as the distance between the atoms placed at $\mathbf{R}_1$ and $\mathbf{R}_3$ for the case of linear molecules. The state describing the time evolution of a three-center molecule can be written as $|\Psi(t)\rangle = e^{iI_p t}[a(t)|0\rangle + \sum_{j=1}^{3}\int d^3\mathbf{v}\, b_j(\mathbf{v},t)|\mathbf{v}\rangle]$, where the subscript $j = 1,2,3$, refers to the contributions of the spatially localized nuclei at $\mathbf{R}_1$, $\mathbf{R}_2$, and $\mathbf{R}_3$, respectively. By employing the TDSE on that state and our basic SFA approach, the molecular time-dependent dipole moment $\vec{\mu}_{3N}(t)$ reads as

$$\vec{\mu}_{3N}(t) = \int d^3\mathbf{v}\,\mathbf{d}^*_{3N}(\mathbf{v})b(\mathbf{v},t) + \text{c.c.} \quad (18)$$

$\vec{\mu}_{3N}(t)$ is defined as a superposition of the bound-continuum dipole matrix of each atom on the molecule, i.e., $\mathbf{d}_{3N}(\mathbf{v}) = \sum_{j=1}^{3}\mathbf{d}_j(\mathbf{v})$. The exact dependency of the bound-continuum matrix element is presented in the Appendix [see Eq. (A32) for more details].

Using the exact definition of the bound-continuum matrix element, the total continuum states transition amplitude $b(\mathbf{v},t) = \sum_{j=1}^{3} b_{0,j}(\mathbf{p},t)$ reads as

$$b(\mathbf{p},t) = i\sum_{j=1}^{3}\int_0^t dt'\,\mathbf{E}(t')\cdot\mathbf{d}_j[\mathbf{p} + \mathbf{A}(t')] \times e^{-i\{S(\mathbf{p},t,t')+\mathbf{R}_j\cdot[\mathbf{A}(t)-\mathbf{A}(t')]\}}. \quad (19)$$

The explicit expression for the molecular time-dependent dipole moment $\vec{\mu}_{3N}(t)$ is obtained inserting Eq. (19) in (18). As in the case of diatomics, it is also possible here to disentangle each of the recombination processes contributing to the total HHG spectrum. In order to do so, we write $\vec{\mu}_{3N}(t)$ as a sum of nine terms as

$$\vec{\mu}_{3N}(t) = \sum_{j=1}^{3}\sum_{j'=1}^{3}\vec{\mu}_{jj'}(t). \quad (20)$$

The above equation contains information about all the possible recombination scenarios present in our three-center molecule. In order to make clearer the interpretation, let us write the individual time-dependent dipole moments $\vec{\mu}_{jj'}(t)$ explicitly as

$$\vec{\mu}_{jj'}(t) = i\int_0^t dt'\left(\frac{\pi}{\varepsilon + \frac{i(t-t')}{2}}\right)^{\frac{3}{2}} \mathbf{E}(t')\cdot\mathbf{d}_j[\mathbf{p}_s + \mathbf{A}(t')] \times e^{-i\{S(\mathbf{p}_s,t,t')+\mathbf{R}_j\cdot[\mathbf{A}(t)-\mathbf{A}(t')]\}}\,\mathbf{d}^*_{j'}[\mathbf{p}_s + \mathbf{A}(t)], \quad (21)$$

where the subscripts j and j' refer to the positions $\mathbf{R}_1$, $\mathbf{R}_2$, and $\mathbf{R}_3$ of each of the atoms in the three-center molecule. In Eq. (21), the first subscript j represents the atom from where the electron is detached and can be $j = 1,2,3$. In addition, the second one j' labels the atom where the recombination process occurs, and can also take the values 1, 2, or 3.

Note that, as in the case of atoms and diatomic molecules, in Eq. (21) we have applied the saddle-point method in the integral over the momentum $\mathbf{p}$ variable. Additionally, we use the conventional saddle-point momentum $\mathbf{p}_s$ following the same criteria as in the diatomic system (see Sec. II B).

As in the case of diatomics, the nine terms of Eq. (20) represent all the possible *local* and *cross* processes. These different terms should be understood as follows:

(i) The first term, $\vec{\mu}_{11}(t)$, describes the process where an electron is laser ionized from the atom placed at $\mathbf{R}_1$ at time t' with probability $\mathbf{E}(t')\cdot\mathbf{d}_1[\mathbf{p}_s + \mathbf{A}(t')]$. This electron, during its excursion in the continuum, accumulates a phase which depends on the position from where it was detached, in this case $\mathbf{R}_1$. Finally, because the change in the sign of the laser electric field, the electron returns to the vicinity of the parent ion and has certain probability of recombination given by $\mathbf{d}^*_1[\mathbf{p}_s + \mathbf{A}(t)]$. As a result of this recombination stage the energy excess acquired from the laser electric field is converted into a high-energy photon. As an example, the time-dependent dipole moment describing this process when $j = 1$ and $j' = 1$ reads as

$$\vec{\mu}_{11}(t) = i\int_0^t dt'\left(\frac{\pi}{\varepsilon + \frac{i(t-t')}{2}}\right)^{\frac{3}{2}} \mathbf{E}(t')\cdot\mathbf{d}_1[\mathbf{p}_s + \mathbf{A}(t')] \times e^{-i\{S(\mathbf{p}_s,t,t')+\mathbf{R}_1\cdot[\mathbf{A}(t)-\mathbf{A}(t')]\}}\,\mathbf{d}^*_1[\mathbf{p}_s + \mathbf{A}(t)]. \quad (22)$$

(ii) The second and third terms, $\vec{\mu}_{22}(t)$ and $\vec{\mu}_{33}(t)$, describe the same process as in (i), but for atoms located at $\mathbf{R}_2$ and $\mathbf{R}_3$, respectively. These three processes are spatially localized: the electron starts and ends at the same point, the same ion core. We then refer to them as *local* processes.

(iii) From the fourth to the seventh terms we have the *cross* processes with the closer neighbor in one and other direction. In this case, notice that in our reference frame, the second atom is placed at $\mathbf{R}_2 = 0$. These processes are understood as in the diatomic case.

(iv) The last two terms are also *cross* processes. For instance, the eighth term can be understood as follows: one electron tunnel ionizes from the atom located at $\mathbf{R}_1$ with probability $\mathbf{E}(t') \cdot \mathbf{d}_1[\mathbf{p}_s + \mathbf{A}(t')]$. This electron starts to move under the influence of the laser electric field and acquires a phase $e^{-i\{S(\mathbf{p}_s,t,t')+\mathbf{R}_1\cdot[\mathbf{A}(t)-\mathbf{A}(t')]\}}$. It then recombines at time t with the farthest ion core at $\mathbf{R}_3$ with an amplitude $\mathbf{d}_3^*[\mathbf{p}_s + \mathbf{A}(t)]$. The last term is understood in a similar way, but inverting the tunnel ionization and recombination positions.

For our three-center molecular system, it is also possible to group the processes as *local* and *cross*. As in the diatomic case, the sum of all these terms represents the total time-dependent dipole element $\vec{\mu}_{3N}(t) = \vec{\mu}_{3N\text{-local}}(t) + \vec{\mu}_{3N\text{-cross}}(t)$. In the same way, we can split the contributions depending on the excursion of the electron in the continuum before recombination. The shorter excursions are represented by the *local* processes where only one atom is involved. For the *cross* processes, we have two possibilities: the recombination with (i) the closest neighbor or (ii) with the farthest one. Those contributions are denoted by

$$\vec{\mu}_{3N\text{-local}}(t) = \vec{\mu}_{11}(t) + \vec{\mu}_{22}(t) + \vec{\mu}_{33}(t) \tag{23}$$

and

$$\vec{\mu}_{3N\text{-cross}}(t) = \vec{\mu}_{3N\text{-cross}_1}(t) + \vec{\mu}_{3N\text{-cross}_2}(t), \tag{24}$$

where

$$\vec{\mu}_{3N\text{-cross}_1}(t) = \vec{\mu}_{12}(t) + \vec{\mu}_{21}(t) + \vec{\mu}_{23}(t) + \vec{\mu}_{32}(t) \tag{25}$$

and

$$\vec{\mu}_{3N\text{-cross}_2}(t) = \vec{\mu}_{13}(t) + \vec{\mu}_{31}(t). \tag{26}$$

In order to describe the *local* processes, we set $j = j'$. For instance, the *local* process for the *right* atom located at $\mathbf{R}_1$ is described by the time-dependent dipole moment $\vec{\mu}_{11}(t)$. On the other hand, the *cross* processes are those where $j \neq j'$.

Finally, in order to compute the total time-dependent dipole moment $\vec{\mu}_{3N}(t)$ of our three-center molecule, we need to evaluate each of the contributions defined by Eq. (21). The HHG spectrum can then be obtained by Fourier transforming $\vec{\mu}_{3N}(t)$ [see Eq. (3)]. The separation of the time-dependent dipole moment allows us to compute the HHG spectrum from each process separately as we will see in the next sections.

III. RESULTS AND DISCUSSION

In this section, we calculate HHG spectra for different atomic and molecular systems using the approach presented above. In addition, we compare the HHG spectra from hydrogen and argon atoms computed with our model with those obtained using the exact numerical solution of the 3D-TDSE. A scan over different laser wavelengths and peak intensities is performed in order to verify and validate our approach. In a second stage, we apply the molecular version of our model to two prototypical diatomic systems: H_2^+ and H_2. We display and study the contributions coming from the *local* and *cross* recombination processes. This analysis helps us to distinguish which contributions interfere constructively or destructively to the total HHG spectra. Finally, we present results for more complex molecules: CO_2 and H_2O. For these cases, aside from disentangling the different contributions to the HHG spectra, we analyze the influence of the angular orientation.

The numerical integration of Eqs. (7), (16), and (21) has been performed by employing a rectangular rule with dedicated emphasis on the results convergence. For all the studied cases, the HHG process is driven by an ultrashort laser pulse with an electric field of the form

$$\mathbf{E}(t) = \mathcal{E}_0\ f(t) \sin(\omega_0\, t + \phi_0)\, \mathbf{e}_z. \tag{27}$$

The field has a carrier frequency $\omega_0 = \frac{2\pi c}{\lambda_0}$, where c is the speed of light ($c \approx 137$ a.u.), and λ_0 the central laser wavelength. In addition, $\mathcal{E}_0$ is the field peak amplitude, linearly polarized in the z axis. $f(t) = \sin^2(\omega_0 t/2N_c)$ denotes the pulse envelope, with N_c the total number of cycles, and the parameter ϕ_0 is the carrier envelope phase (CEP). Under the dipole approximation, the influence of the magnetic field component of the laser field is neglected.

A. Atomic systems: Comparison between SFA and 3D-TDSE models

The HHG spectra of a hydrogen atom is performed by Fourier transforming the time-dependent dipole moment presented in Eq. (7). We set $\Gamma = 1$ and $\gamma = 38$ a.u. in our nonlocal SR potential in order to match the hydrogen ionization potential $I_p = 0.5$ a.u. The HHG spectra at different laser wavelengths and using our quasiclassical SFA model are shown in Fig. 1(a). In addition, in Fig. 1(b) we show the HHG spectra obtained by using the numerical solution of the 3D-TDSE.

In order to compute the HHG spectra displayed in Fig. 1, we consider the laser pulse described by Eq. (27), with a laser peak intensity of $I_0 = 1.58 \times 10^{14}$ W cm^{-2} and different laser wavelengths (see the panels' labels for details). Additionally, we set $N_c = 4$ and $\phi_0 = 0$ rad. A total of 131 072 points in the time window $t \in [0, t_F]$, where $t_F = N_c T_0$ and $T_0 = 2\pi/\omega_0$, are used during the numerical integration. The HHG spectra of Fig. 1(b) are obtained by numerically solving the 3D-TDSE in the length gauge. Thus, by Fourier transforming the dipole acceleration, calculated from the time-propagated electronic wave function, the HHG spectra are obtained. We have used our code, which is based on an expansion in spherical harmonics, Y_{lm} considering only the $m = 0$ terms due to the cylindrical symmetry of the problem. The numerical technique to solve the 3D-TDSE is based on a Crank-Nicolson scheme implemented on a splitting of the time-evolution operator that preserves the norm of the electronic wave function.

Both panels of Fig. 1 reveal the typical HHG behavior, namely, (i) a rapidly decreasing of the harmonic yield for the lower harmonic orders (<10th), (ii) a plateau with almost constant yield, and (iii) an abrupt end at the so-called HHG cutoff. The cutoff energy is one of the most important features

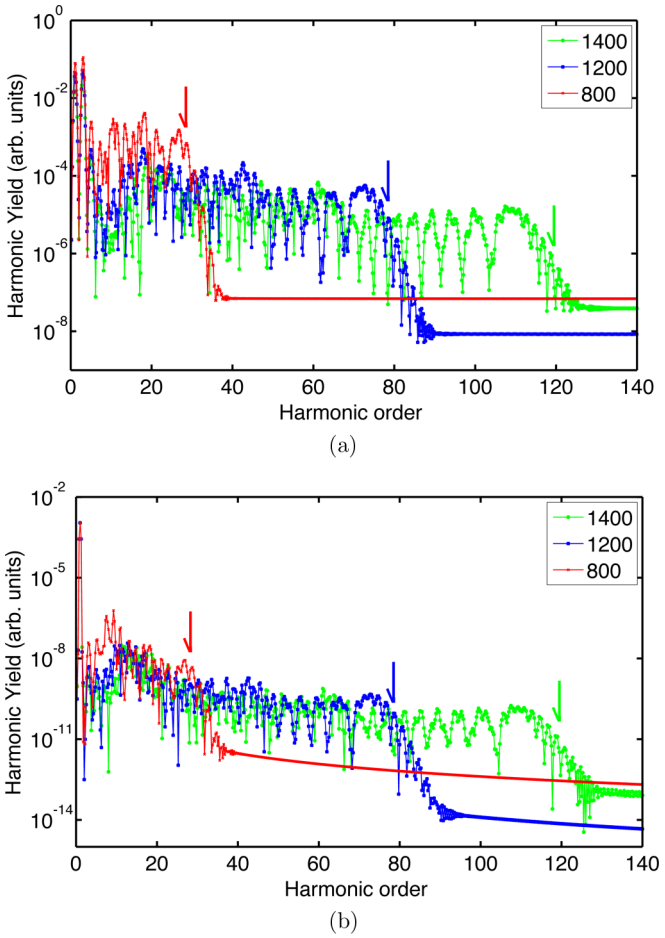

FIG. 1. HHG spectra $I_{1N}(\omega)$ (in logarithmic scale) of hydrogen driven by a strong few-cycle pulse at different wavelengths. $\lambda_1 = 800$ nm (red asterisk line), $\lambda_2 = 1200$ nm (blue square line), and $\lambda_3 = 1400$ nm (green circle line). (a) Quasiclassical SFA model; (b) 3D-TDSE. The arrows in all the panels indicate the position of the classical HHG cutoff (see the text for details).

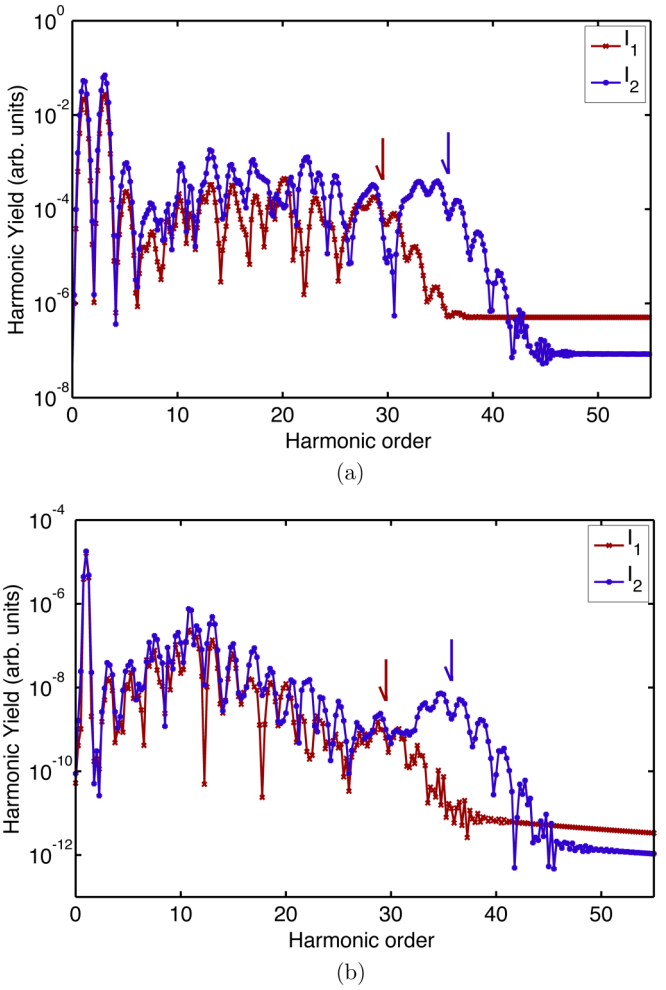

FIG. 2. HHG spectra $I_{1N}(\omega)$ (in logarithmic scale) of Ar driven by a strong few-cycle pulse with $\lambda = 800$ nm, at different laser peak intensities. (a) Our quasiclassical SFA at $I_1 = 1.58 \times 10^{14}$ W cm^{-2} (red square line) and $I_2 = 2.08 \times 10^{14}$ W cm^{-2} (blue cross line); (b) same as in (a) but solving the 3D-TDSE. Note that in this case the minimum in the efficiency around the 27th harmonic is the Cooper minimum in Ar. The arrows in all the panels indicate the position of the classical HHG cutoff (see the text for details).

of any HHG spectrum. It can be defined as the maximum photon energy that can be released at recollision. Classically, it is possible to prove that [14,15]

$$\omega_{\text{cutoff}} = I_p + 3.17\, U_p, \tag{28}$$

where ω_{cutoff} is the maximum photon energy and $U_p = I_0/4\omega_0^2$ is the ponderomotive energy. As can we see from Fig. 1, both the SFA and 3D-TDSE calculations show the expected classical cutoff defined by Eq. (28), noted with an arrow at $\omega_{\text{cutoff }800} = 1.59$ a.u. (43.26 eV), $\omega_{\text{cutoff }1200} = 2.97$ a.u. (80.8 eV), and $\omega_{\text{cutoff }1400} = 3.87$ a.u. (105.3 eV), respectively. From Eq. (28) we should notice that $\omega_{\text{cutoff}} \propto I\lambda^2$ and this behavior can also be observed in Fig. 1. For instance, the spectra at $\lambda_3 = 1400$ nm have a cutoff energy about four times higher than the one calculated using a wavelength of $\lambda_1 = 800$ nm.

A natural next step would be to test our model with a more complex atom. In order to do so, in Fig. 2 we show HHG spectra for an argon atom, calculated both with (i) our quasiclassical SFA [Fig. 2(a)] and (ii) using the numerical solution of the 3D-TDSE under the SAE approximation [Fig. 2(b)]. We employ two different laser peak intensities and using a laser pulse with a central frequency of $\omega_0 = 0.057$ a.u., that corresponds to a wavelength of about 800 nm. As in the previous case, we confirm that our model is capable to capture not only the dependency of the harmonic spectra with the wavelength, but also with the laser peak intensity. As we can see, and considering that $I_2 > I_1$, a clear cutoff extension in the HHG spectra for I_2 is observed. A remarkable good agreement between both methods is clearly seen in Fig. 2 and for both laser peak intensities.

The HHG spectra presented both for a single-electron system (H, Fig. 1) and a complex target (Ar, Fig. 2) reveal the very good agreement between our quasiclassical SFA model and the numerical solution of the 3D-TDSE.

B. Diatomic molecular systems

In this section, we calculate HHG spectra for two prototypical diatomic molecules: H_2^+ and H_2.

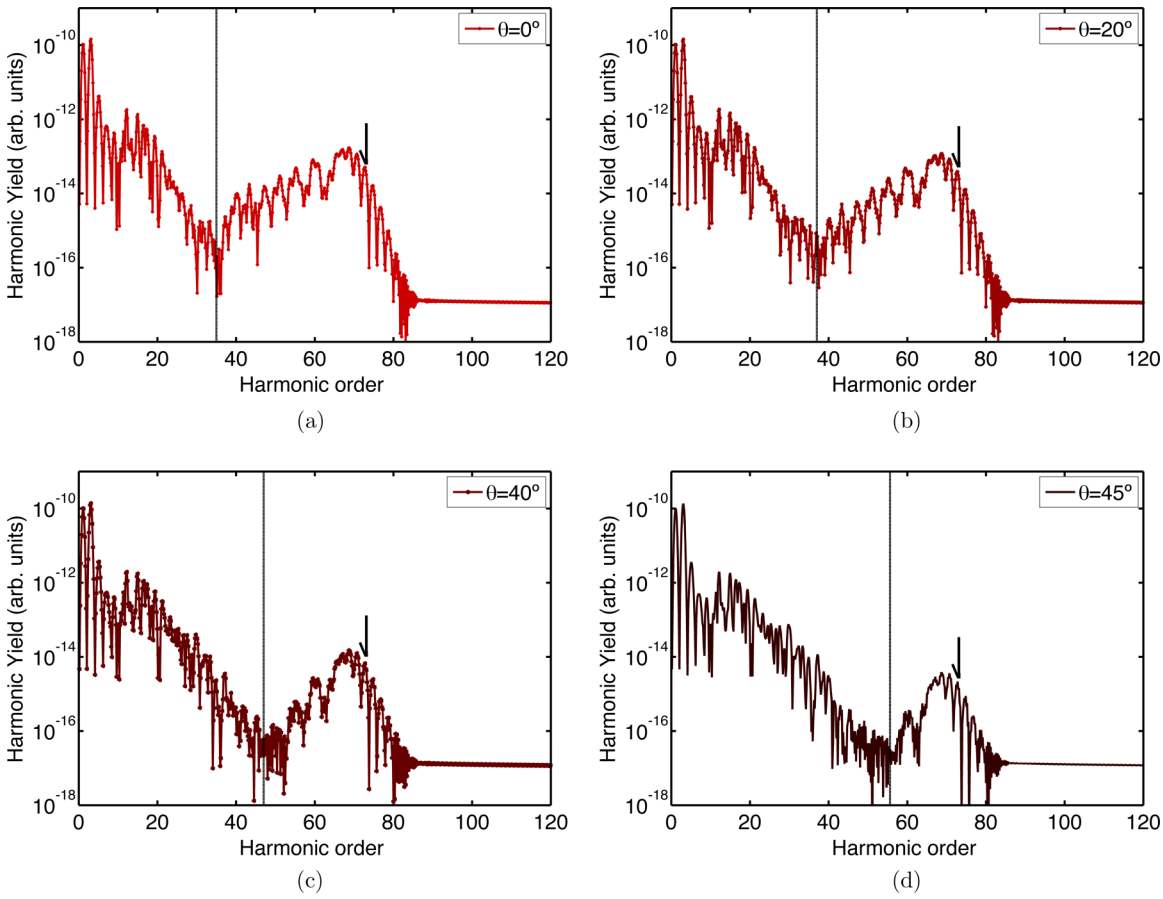

FIG. 3. Total harmonic spectra $I_{2N}(\omega)$ (in logarithmic scale) [Eq. (3)] of an H_2^+ molecule driven by a strong few-cycle pulse as a function of the harmonic order computed using our quasiclassical SFA. (a) HHG for an H_2^+ molecule aligned with the laser-pulse polarization axis, i.e., $\theta = 0°$; (b) the same as (a) but for $\theta = 20°$; (c) the same as (a) but for $\theta = 40°$; (d) the same as (a) but for $\theta = 45°$. The vertical lines indicate the position of the interference minima of our quasiclassical SFA model and the arrows in all the panels the position of the classical HHG cutoff (see the text for details), respectively.

1. H_2^+ molecule

Figure 3 shows the numerically computed HHG spectra for an H_2^+ molecule by using the quasiclassical SFA model presented in Sec. II B. The H_2^+ system is modeled by two identical centers separated by an internuclear distance $R = 2.2$ a.u. (1.16 Å) and the molecular axis forms a θ angle with respect to the incident laser electric field polarization, i.e., $\mathbf{R} = (0,0,R\cos\theta)$. The parameters of our nonlocal SR potential are set to $\Gamma = 1.0$ and $\gamma = 0.1$ a.u. in order to reproduce the minimum at the equilibrium internuclear distance, $R_0 = 2.0$ a.u. (1.06 Å), in the potential energy surface (PES). The total ionization potential extracted from the potential energy surface in our model yields $I_p = 0.68$ a.u. (18.50 eV). This electronic ground-state energy allows us to fix the correct asymptotic behavior of the H_2^+ PES (see Ref. [40] for more details). Note that this last value differs from the one obtained with a real Coulomb potential that leads a pure electronic energy of 1.1 a.u. (30 eV) approximately.

The incident laser field shape is identical to the one used in the atomic case and has a central frequency $\omega_0 = 0.057$ a.u., corresponding to a wavelength $\lambda = 800$ nm and photon energy of 1.55 eV. The total number of cycles is $N_c = 4$ [this defines a full-width at half-maximum (FWHM) value of 5.2 fs] and $\phi_0 = 0$ rad. The time step is set to $\delta t = 0.032$ a.u. and this corresponds to a total of $N_t = 20\,000$ points for the numerical integration. The time window is $t \in [0, t_F]$, where $t_F \approx 11$ fs denotes the final time, i.e., the end of the laser electric field pulse. Finally, the laser peak intensity is set to $I_0 = 5 \times 10^{14}$ W cm^{-2}.

In Fig. 3, we display results for a scan of four different molecular orientations, namely, Fig. 3(a) $\theta = 0°$ (this value corresponds to the so-called parallel alignment), Fig. 3(b) 20°, Fig. 3(c) 40°, and Fig. 3(d) 45°, respectively. As we can see in all the panels an absolute minimum over the total HHG spectra is clearly visible and the harmonic order where these minima are located increases with the orientation angle. The existence of those minima and their dependency with the alignment angle can be explained by invoking an interference phenomenon as we will see below. In the most simplest picture, the minima appear as a consequence of the harmonic emission of two radiant points (see, e.g., [9] for more details).

According to the equation describing the destructive interference of two radiant sources, $R\cos\theta = (2m+1)\lambda_k/2$, where λ_k is the de Broglie wavelength of the returning electron and considering the "fundamental" instance $m = 0$,

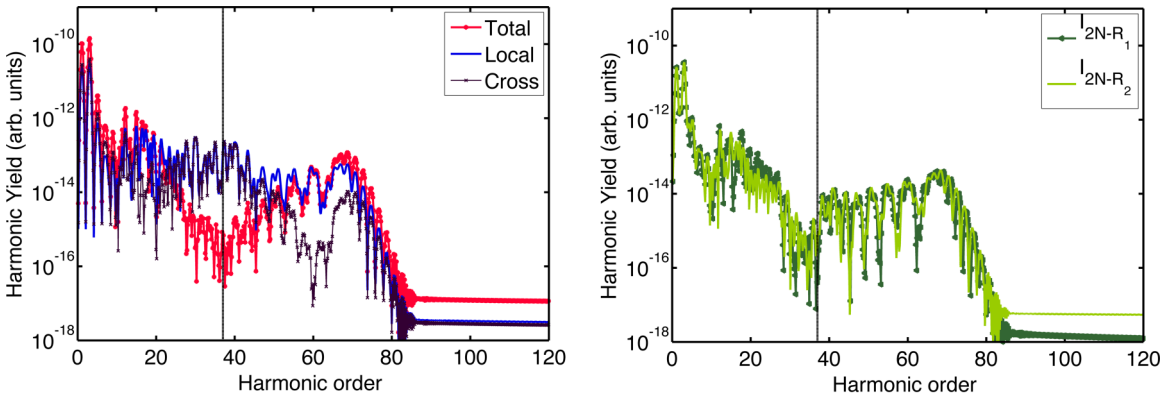

FIG. 4. Harmonic spectra $I_{2N}(\omega)$ (in logarithmic scale) of an H_2^+ molecule [Eq. (3)] as a function of the harmonic order calculated using our quasiclassical SFA and for an orientation angle $\theta = 20^\circ$. (a) Local, cross, and total contributions to the HHG spectrum; (b) contributions depending on the recombination atom. Green circle line: recombination at $\mathbf{R}_1$ and light green line: recombination at $\mathbf{R}_2$. The vertical lines indicate the position of the interference minima (see the text for details).

the minima should be located at the 18th, 20th, 30th, and 36th harmonic order for $\theta = 0^\circ$, 20°, 40°, and 45°, respectively. The positions of the minima in our SFA calculation are ≈35th, ≈37th, ≈45th, and ≈54th, respectively (see the vertical lines in all the panels of Fig. 3). We speculate that the shifts in harmonic frequency are related with the kind of potential used in our calculations; the nonlocal SR potential does not correctly describe the low-energy part of the HHG spectra, where the Coulomb potential plays an important role [32]. We note, however, that our SFA calculation for $\theta = 40^\circ$ is in excellent agreement with the numerical solution of the 2D-TDSE and 3D-TDSE for the H_2^+ molecule [9,31]. Lastly, we observe that in all the HHG spectra of Fig. 3 the position of the classical cutoff is in excellent agreement with Eq. (28) (see the arrows in all the panels of Fig. 3). Particularly, for our H_2^+ molecular system and the laser parameters used in our simulations, the cutoff frequency is $\omega_{\text{cutoff}} = 4.15$ a.u. (112.92 eV), corresponding to the 72th harmonic order.

Clearly, our quasiclassical molecular SFA model has drawbacks and advantages. The first advantage is from the computational viewpoint; the numerical calculations using our SFA approach are much faster than the numerical solution of the 3D-TDSE. The computation of one single HHG spectrum for a set of fixed parameters takes few seconds. The second, and might be the most important one, is the possibility to disentangle the different processes contributing to the final HHG spectra (see Sec. II B). In order to do so, in Fig. 4 we plot the different contributions for an H_2^+ molecule aligned at $\theta = 20^\circ$ with respect to the laser field polarization. Figure 4(a) shows the total $I_{2N}(\omega)$ (red circle line), the *local* $I_{2N\text{-local}}(\omega)$ (blue line), and the *cross* $I_{2N\text{-cross}}(\omega)$ (dark brown asterisk line) contributions (for details see Sec. II B). As we can see from this picture, the two-center destructive interference is not present either in the *local* or in the *cross* contributions. The latter have a deep minimum but at a different position, about the 60th harmonic order, while the former remains almost constant in yield for all the harmonic frequencies. In order to trace out the origin of the two-center destructive interference present in the total HHG spectra in Fig. 4(b) we plot the contributions depending on the recombination atom, calculated as

$$I_{2N\text{-}R_1}(\omega) \propto \left| \int_{-\infty}^{\infty} dt\, e^{i\omega t}\, [\vec{\mu}_{11}(t) + \vec{\mu}_{21}(t)] \right|^2 \tag{29}$$

and

$$I_{2N\text{-}R_2}(\omega) \propto \left| \int_{-\infty}^{\infty} dt\, e^{i\omega t}\, [\vec{\mu}_{22}(t) + \vec{\mu}_{12}(t)] \right|^2. \tag{30}$$

From this figure we can clearly see that there is a deep minimum for both terms and it is located at the same position as for the total HHG spectrum. It means that, for the case of the recombination on $\mathbf{R}_1$ (dark green circle line), the electron wave packet ionized at $\mathbf{R}_1$ interferes with the one coming from $\mathbf{R}_2$ and the other way around. These minima are then generated by the destructive interference of such electron wave packets. From the drawbacks side, we have seen that our nonlocal SR potential is unable to accurately reproduce the interference minima positions for some of the molecular orientation angles. We note, however, that these minima are typically washed out when an average over the molecular orientation is considered, configuration that is commonly used in molecular HHG experiments.

2. *Time-frequency analysis for H_2^+*

We have seen in Fig. 4 that the independent processes $\vec{\mu}_{11}(t)/\vec{\mu}_{22}(t)$ and $\vec{\mu}_{21}(t)/\vec{\mu}_{12}(t)$ are the ones interfering and creating the deep minimum in the total HHG spectra. In order to dig deeper about the existence of this distinctive feature, a Gabor analysis [45,46] over the different contributions is displayed in Fig. 5. The Gabor transformation was performed upon the time-dependent dipole moment calculated using our quasiclassical SFA model. The laser parameters are the same as in Fig. 4.

This time-frequency analysis allows us to reveal the half-cycle bursts of radiation from which the HHG spectrum is formed and the main trajectories contributing. In Figs. 5(a) and 5(b), we show the *local* and *cross* processes at $\mathbf{R}_1$, $\vec{\mu}_{11}(t)$, and $\vec{\mu}_{21}(t)$, respectively (note that identical plots can be obtained by changing $\mathbf{R}_1$ by $\mathbf{R}_2$). As we can observe from these figures,

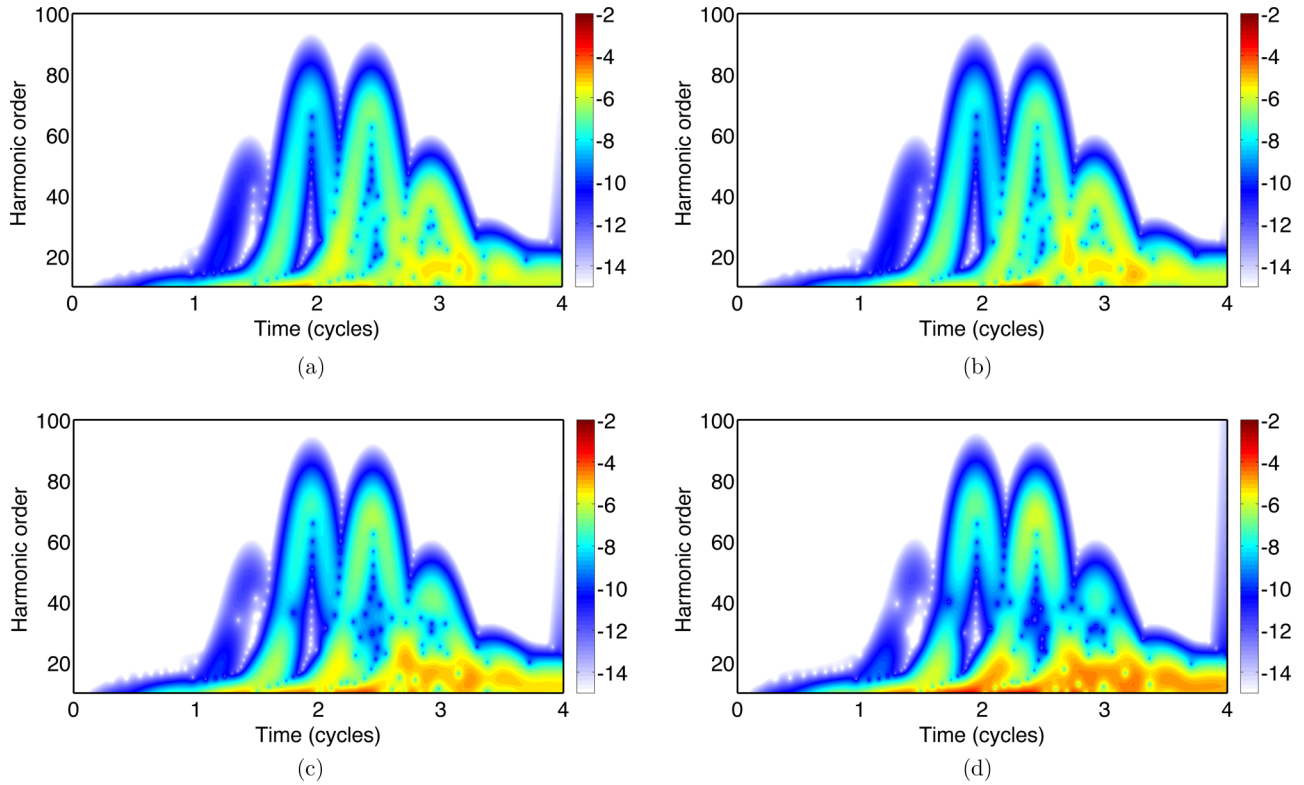

FIG. 5. Gabor transformation of the time-dependent dipole moment of an H_2^+ diatomic molecule oriented $\theta = 20^\circ$ with the laser field. (a) *Local* processes at $\mathbf{R}_1$ using the time-dependent dipole moment $\vec{\mu_{11}}(t)$; (b) the same as (a) but for the *cross* processes $\vec{\mu_{21}}(t)$; (c) the same as (a) but for all the recombination processes at $\mathbf{R}_1$, i.e., $\vec{\mu_{11}}(t) + \vec{\mu_{21}}(t)$; (d) Gabor transformation for the total time-dependent dipole moment $\vec{\mu}_{2N}(t)$.

they both look almost equal and similar to the atomic case. In both cases, we have the contribution of the short and long trajectories. For the earlier cycles, the first and second ones, the short trajectory contributions dominate while for the latest cycles both long and short trajectories have the same weight. The main differences between these two contributions are in the low-energy region around the end of the laser pulse, the third optical cycle, where the contribution of the *cross* processes $\vec{\mu}_{21}(t)$ is slightly higher than the *local* ones.

Finally, we plot in Fig. 5(c) all the recombination processes contributions at $\mathbf{R}_1$, i.e., $\vec{\mu_{11}}(t) + \vec{\mu_{21}}(t)$ and in Fig. 5(d) the total contributions. From these figures is evident the presence of an interference minimum for the whole temporal window. This means that the $\vec{\mu}_{11}(t)$ and $\vec{\mu}_{21}(t)$ processes, that describe electrons arriving at the same point $\mathbf{R}_1$ from two different atomic sources $\mathbf{R}_1$ and $\mathbf{R}_2$, respectively, cancel each other and an interference zone is seen for an harmonic order of around 35th. These two contributions are dominated by the short trajectories, therefore, both incoming electron wave packets arrive at the same time and as a consequence a destructive interference is observed. This feature is inherited to the total time-dependent dipole moment [see Fig. 5(d)].

3. H_2 molecule

The next simplest diatomic molecule is H_2. In order to investigate the behavior and versatility of our semiclassical SFA model, we compute HHG spectra using the time-dependent dipole moment presented in Sec. II. We consider an H_2 molecule in equilibrium where the two H atoms are separated a distance of $R = 1.4$ a.u. (0.74 Å). The ionization potential of the outer electron predicted by our nonlocal SR potential is $I_p = 1.5$ a.u. (40.82 eV) and it was calculated by setting $\Gamma = 1.0$ and $\gamma = 0.12$ a.u. With these parameters our model reproduces the PES of H_2 with a minimum at the equilibrium internuclear distance [8]. The driven laser pulse has the same parameters as for the case of H_2^+.

Figure 6 shows the different contributions to the total HHG spectrum by considering two different molecular orientations: parallel, $\theta = 0^\circ$ [Fig. 6(a)] and perpendicular, $\theta = 90^\circ$ [Fig. 6(b)] with respect to the incident laser-pulse polarization. The total HHG spectrum (in red) is computed as the sum of all possible processes (see Sec. II B for details). In both panels, we have grouped two main contributions: (i) the *local* and (ii) the *cross* ones. The *local* contributions (blue line) are processes related with only one atom or position, i.e., they involve the sum of processes involving only one single atom, meaning ionization from the $\mathbf{R}_1/\mathbf{R}_2$ and recombination at the same atom. On the other hand, the *cross* contributions (in dark brown) include processes involving both of the atoms in the molecule, i.e., ionization from the atom located at $\mathbf{R}_1$ and recombination on the atom located at $\mathbf{R}_2$ and the other way around.

The first observation regarding Fig. 6 is that for the case of parallel orientation [Fig. 6(a)], the total HHG spectrum starts to gradually decrease for harmonic orders higher than the ≈30th. This behavior is due to a destructive interference of the *local*

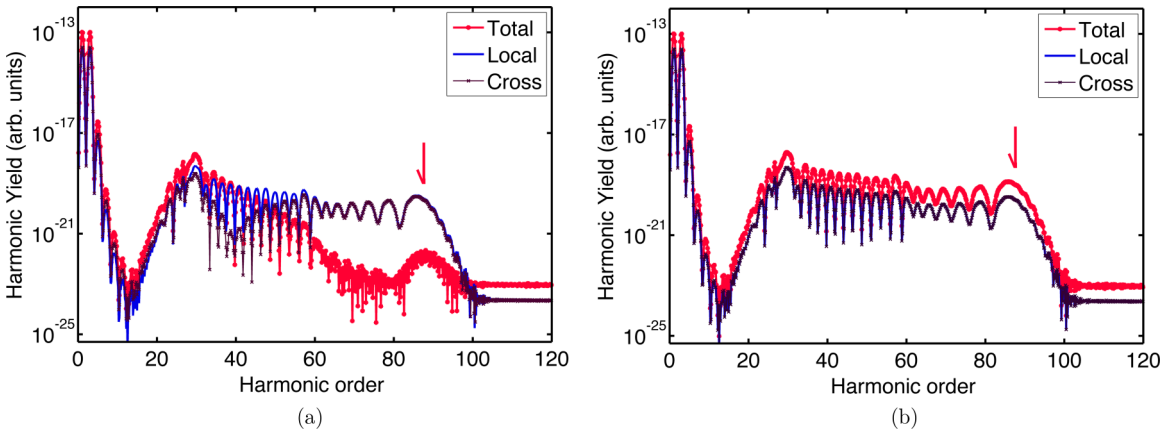

FIG. 6. Different contributions to the molecular HHG spectrum (in logarithmic scale) for an H_2 molecule. (a) Total, *local*, and *cross* contributions for a molecule oriented parallel ($\theta = 0^\circ$) to the laser field polarization; (b) the same as in (a) but for $\theta = 90^\circ$ (perpendicular orientation).

and the *cross* processes. The latter shows a deep minimum around the ≈40th harmonic order. In the case of the molecule perpendicularly oriented [Fig. 6(b)], an extended plateau with a cutoff around the 90th harmonic order is clearly visible. In both cases, parallel and perpendicular, the molecular HHG spectra show a deep minimum around the 12th harmonic order. As in the case of H_2^+ previously presented, the utilization of a nonlocal SR potential restricts our results to the higher-order harmonics, where the influence of the molecular potential details is less relevant.

It is interesting to note that for the case of perpendicular orientation $\theta = 90^\circ$ [Fig. 6(b)], both the *local* and *cross* processes contribute evenly in the plateau region of the HHG spectra, while for the parallel orientation $\theta = 0^\circ$ [Fig. 6(a)], both present a different behavior. We can then infer that for the $\theta = 90^\circ$ case, the total HHG spectrum reaches a maximum yield at the cutoff region. This is due to the fact that, for this favorable orientation, the contribution of each of the processes, *local* and *cross*, is comparable.

Finally, in Fig. 7, we show the total HHG spectra for three different molecular orientations $\theta = 0^\circ$, 45°, and 90° and an averaged case over nine values of θ in the range [0°–360°]. Our diatomic molecule is symmetrical with respect to the origin, i.e., $\mathbf{R}_1 = -\mathbf{R}/2$ and $\mathbf{R}_2 = \mathbf{R}/2$ and, consequently, the total HHG spectra for $\theta = 0^\circ$ and 180° are identical. The same behavior is observed for the spectra at 45°, 135°, 225°, and 315° or for 90° and 270°. We can observe in Fig. 7 how different molecular configurations contribute to the total HHG spectra. As we can see, the difference in the total HHG spectra for different orientation angles is hardly to notice for lower harmonic orders (<30th). Differences start to be noticeable in the mid-plateau and cutoff regions. In these zones, the highest HHG yield is reached for the perpendicular orientation ($\theta = 90^\circ$), thus confirming the results presented in Fig. 6. Two final remarks are in order, namely, (i) the averaged total HHG spectrum is about one order of magnitude lower than the one at perpendicular orientation; (ii) the average procedure washes out any two-slit interference fingerprint.

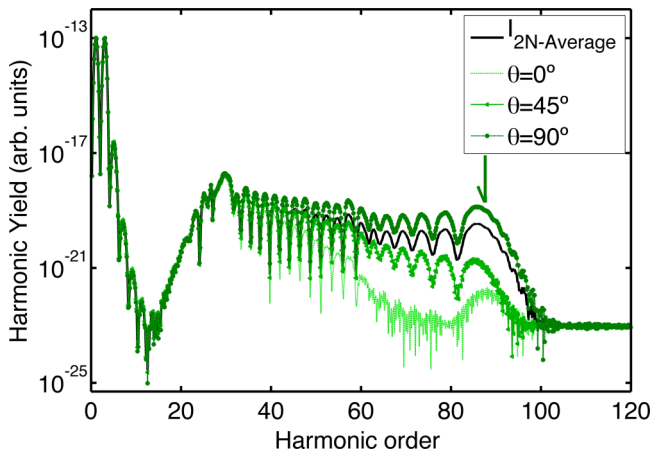

FIG. 7. Total H_2 molecular HHG spectra (in logarithmic scale) for $\theta = 0^\circ$, 45°, 90° and averaged over nine different molecular orientations (see the text for more details).

4. *Time-frequency analysis for H_2*

In Fig. 8, we perform a Gabor transformation upon the time-dependent dipole moment for both an H atom and our diatomic H_2 molecule. Our aim with this time-energy analysis is to investigate the influence of the short and long trajectories for the molecular system and highlight the differences with the atomic case. In Fig. 8(a), we show the calculation for the H atom, while in Fig. 8(b) we depict the same analysis for the molecular system randomly oriented. In both cases we have considered a laser peak intensity $I_0 = 5 \times 10^{14}$ W cm^{-2}.

In general, both figures look quite different. The atomic system [Fig. 8(a)] is mostly dominated by the short trajectories while the molecular system [Fig. 8(b)] have a prevailing contribution from the long ones. This is so because the orientation average procedure removes every fingerprint of two-center interferences.

From a detailed comparison between the atomic and molecular cases we observe that for the former, even when the short trajectories are dominant at the beginning of the laser pulse (first two optical cycles), some contribution of the long ones survives for the later optical cycles, where long and short trajectories contributions are similar (three optical cycles).

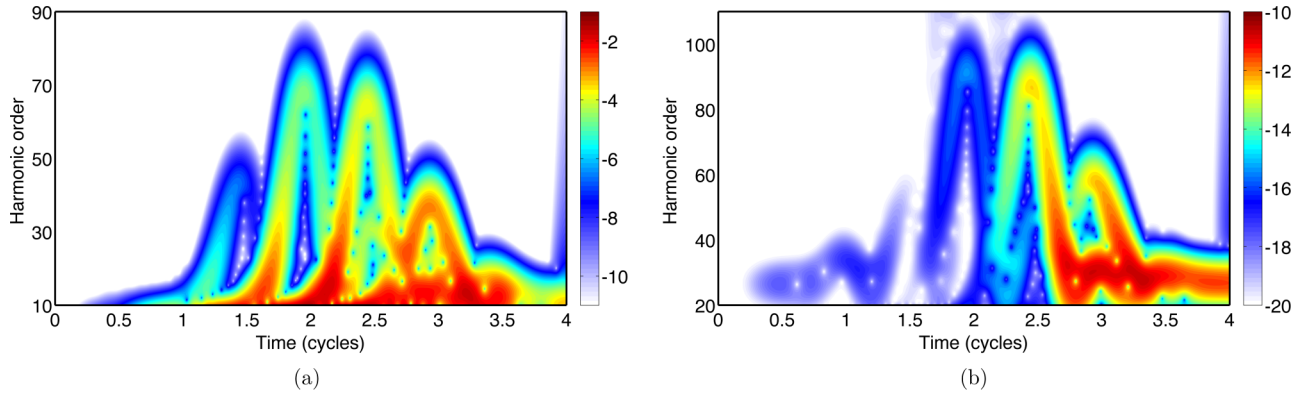

FIG. 8. Gabor transformation of the time-dependent dipole. (a) H atom driven by a laser pulse with a peak intensity of $I_0 = 5 \times 10^{14}$ W cm^{-2}; (b) same as (a) but for an H_2 molecule.

On the contrary, in the molecular system, short and long trajectories contribute to different optical cycles. For instance, in the first and second optical cycles the main contribution is from the short trajectories while for the third and fourth optical cycles a big contribution of the long trajectories appears. In the molecular system, the contributions of the long trajectories start to increase, being paramount for the later optical cycles where the contribution of the short ones is less significant.

C. Three-center molecular systems

In order to study systems with more degrees of freedom and describe the different processes contributing to the total HHG spectra, as we have done for diatomics, we apply the model described in Sec. II C to both CO_2 and H_2O molecules.

1. *Carbon dioxide (CO_2) molecule*

The carbon dioxide molecule CO_2 is a linear system formed by three atoms O = C = O, where the two oxygen atoms are separated by a distance $R = 4.38$ a.u. (2.31 Å), when the system is in equilibrium. Here, to model this state, the parameters of the nonlocal SR potential are set to $\Gamma = 0.8$ and $\gamma = 0.11$ a.u. An ionization potential $I_p = 0.50$ a.u. (13.6 eV) is obtained. This value is in excellent agreement with the actual CO_2 ionization energy (13.77 eV) [47]. The incident laser electric field is defined in Eq. (27) and we use a laser wavelength and peak intensity of $\lambda = 800$ nm and $I_0 = 1 \times 10^{14}$ W cm^{-2}, respectively. The laser pulse has four total cycles (11 fs of total duration) and the CEP is set to $\phi_0 = 0°$.

We present HHG spectra, computed by using our quasiclassical SFA model, for the CO_2 molecule in Fig. 9. In Fig. 9(a), we show the different contributions to the HHG spectra: the total $I_{3N}(\omega)$ (solid line with red circles), calculated from the time-dependent dipole moment presented in Eq. (20), the *local* $I_{3N\text{-local}}(\omega)$ (blue solid line), computed with Eq. (23), and the *cross* $I_{3N\text{-cross}}(\omega)$ (dark brown line with asterisks), extracted from Eq. (24). These calculations show the well-known HHG plateau that ends with a cutoff (marked with a red arrow) at around the 21st harmonic order [this last value is in perfect agreement with the one predicted by the semiclassical law, see Eq. (28)]. Both *local* and *cross* contributions have almost the same yield over all the frequency range and only minor differences are visible.

In Fig. 9(b), we present a split of the *local* processes, namely, $I_{3N\text{-}11}(\omega)$ (solid line with purple circles), $I_{3N\text{-}22}(\omega)$ (solid line with light blue squares), and $I_{3N\text{-}33}(\omega)$ (dashed line). As we can see the contribution from the O atoms, placed at the end of the molecule, is equal in amplitude and shape and different in yield from the $I_{3N\text{-}22}(\omega)$ (corresponding to the C atom placed at the origin). This means that the O atoms contribute a slightly less than the C atom. We notice, however, that the shapes and positions of the minima are the same for the three contributions.

In Fig. 9(c), we present each of the contributions that build up the total *cross* processes. We have separated them depending on how long the laser-ionized electron travels in the continuum before recombination. The cross_1 (solid line with orange circles) [Eq. (25)] and the cross_2 (solid brown line) [Eq. (26)] contributions have similar yields. The main difference between these two HHG spectra is the yield: the cross_1 contribution has a higher yield than the cross_2 one. The position of the absolute minima around the 19th harmonic order is present in both contributions: the same can be seen in the *local* term. For the calculations in Figs. 9(a)–9(c), we consider a CO_2 molecule aligned perpendicular to the incident laser-pulse polarization, i.e., the internuclear axis vector is forming an angle $\theta = 90°$ with respect to the z axis, being this one the most favorable configuration [see Fig. 9(d)].

Finally, in Fig. 9(d) we present a set of total HHG spectra for different molecular orientations, namely, parallel ($\theta = 0°$), oblique ($\theta = 45°$), and perpendicular ($\theta = 90°$). In addition, we include an averaged HHG spectrum, obtained coherently adding four different orientations. We can observe a similar behavior as for the case of H_2 (see Fig. 7), i.e., the difference in the total spectra for different orientation angles is hardly to see for lower harmonic orders and starts to be visible in the mid-plateau and cutoff regions. Furthermore, the perpendicular orientation appears to be the dominant one. The comparable behavior between the CO_2 and H_2 molecules supports the fact that the former could be considered as a *stretched* diatomic O_2 molecule for interference minima calculations [8].

2. *Water (H_2O) molecule*

One of the most important three-center molecules is water (H_2O) since it is an essential part of the blocks that build

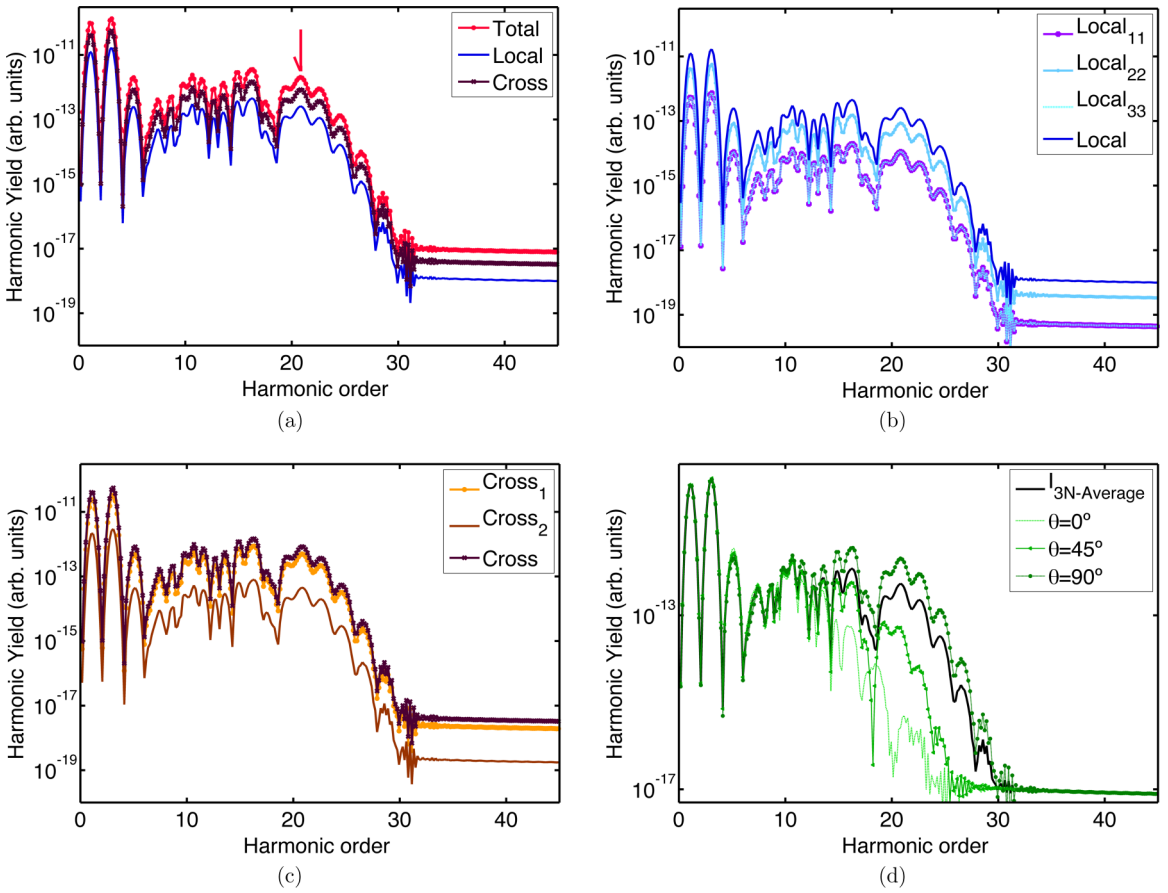

FIG. 9. CO_2 molecular HHG spectra $I_{3N}(\omega)$ (in logarithmic scale) as a function of the harmonic order calculated by using our quasiclassical SFA. In panels (a)–(c) the CO_2 molecule is oriented perpendicular to the laser polarization, i.e., $\theta = 90^\circ$ (see text for more details).

biological life. In this section, we theoretically investigate HHG spectra of the H_2O molecule using our semiclassical SFA approach.

We consider an H_2O molecule under the influence of the strong laser field described by Eq. (27). The H_2O molecule is an angular molecule with two H atoms and one O atom. At equilibrium, the internuclear distance of the bond H = O is about $R = 1.8$ a.u. (0.95 Å) and the angle between the two H atoms $\alpha = 104.5^\circ$. For this configuration, and considering an ionization potential of $I_p = 0.46$ a.u. (12.52 eV) [48], we set the parameters of our nonlocal SR potential to $\Gamma = 0.8$ and $\gamma = 0.1$ a.u.

In Fig. 10, we show HHG spectra for a laser wavelength and peak intensity of $\lambda = 800$ nm and $I_0 = 1 \times 10^{14}$ W cm^{-2}, respectively. The laser pulse has four total cycles (11 fs of total duration) and the CEP is set to $\phi_0 = 0$ rad. In Fig. 10(a), we show HHG spectra both for five different molecular orientations $\theta = 0^\circ$, 20°, 45°, 60°, and 90° and an averaged case. The molecular axis is fixed in space and forms an angle of $\alpha/2$ with respect to the vector position $\mathbf{R}_1$. Furthermore, θ defines the angle between this molecular axis and the laser electric field polarization (see Fig. 12 in the Appendix for more details).

The dependency of the HHG spectra with respect to the molecular orientation is quite evident. For lower harmonic orders, all the orientations appear to be equivalent and the main differences start to materialize for harmonic orders $\gtrsim$12th. As we can see in Fig. 10(a), the HHG spectrum for $\theta = 0^\circ$ (solid line with asterisks), 20° (solid line with left-pointing triangle), and 45° (dashed line) exhibit a similar structure. The other two orientations, 60° (right-pointing triangle line) and $\theta = 90^\circ$ (square line), present an harmonic yield several orders of magnitude lower in this region. The total HHG spectra for all the molecular orientations show a slight minimum around the 17th harmonic order that could be attributed to interference effects, although it is not an easy task to characterize it using a simple interference formula as in the case of diatomics.

We have also included in Fig. 10(a) an averaged HHG spectrum over eight values of θ in the range $[0^\circ$–$360^\circ]$ (dashed red line). As we can see, the minimum survives the orientation average. Furthermore, for $\theta = 90^\circ$ (square line) the total HHG spectrum rapidly decreases for harmonic orders >16th. This means that the interference between the *local* and *cross* processes is destructive and function of the molecular orientation. This behavior introduces a decrease of the total HHG yield. We note that for H_2O, contrarily to the CO_2 case, an enhancement of the total HHG spectrum is observed when the molecule is oriented parallel, $\theta = 0^\circ$, to the laser electric field polarization. As we have done both for diatomics and CO_2 in Fig. 10(b) we plot the different terms contributing to the total HHG averaged spectrum. Contrarily to the oriented case, here the *local* and *cross* processes appear to constructively contribute to the total HHG spectrum.

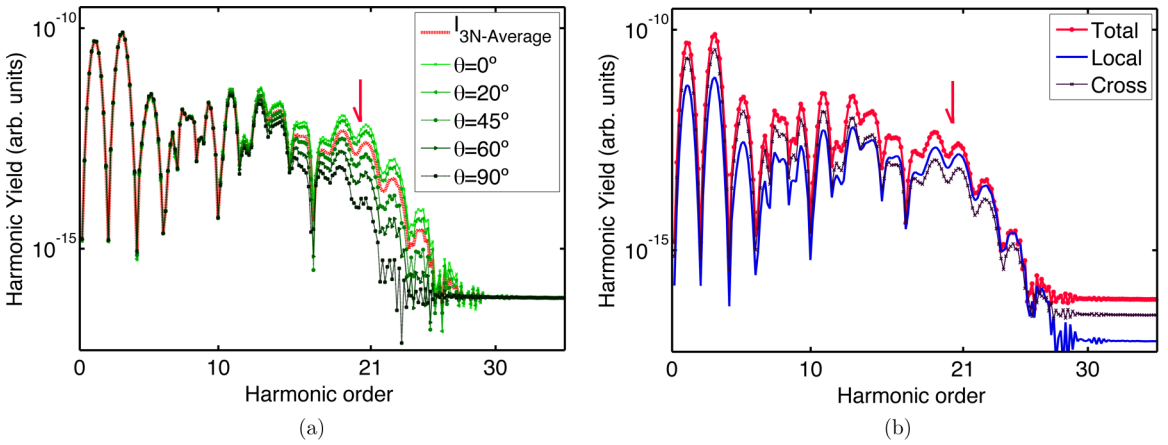

FIG. 10. HHG spectra $I_{3N}(\omega)$ (in logarithmic scale) of an H_2O molecule, as a function of the harmonic order, computed using our quasiclassical SFA model. (a) HHG spectra for $\theta = [0°,20°,45°,60°,90°]$ and averaged over eight orientations in the range $\theta = [0°–360°]$; (b) different contributions to the averaged HHG spectra.

In order to study more deeply the underlying physics behind the enhancement and decrease of the total HHG spectra for 0° and 90°, we plot in Fig. 11 the different contributions for these two particular cases. For $\theta = 0°$ [Fig. 11(a)], the decrease of the HHG yield is evident for harmonic orders higher than the 15th. Around this harmonic order, both contributions, the *local* and *cross*, have a similar yield and the coherent sum develops in a destructive interference decreasing the total HHG spectrum in about three orders of magnitude. On the other hand, for $\theta = 90°$ [Fig. 11(b)], we observe a steady decrease of the *cross* processes, of about two orders of magnitude, in the whole spectral range. Consequently, we can argue that in this case the *cross* contributions are almost negligible (solid brown line with squares) and the total HHG spectra are mainly dominated by the *local* processes (solid blue line).

IV. CONCLUSIONS AND OUTLOOK

We present a quasiclassical approach that deals with molecular HHG within the SAE. Our model could be considered as a natural extension to the one introduced for ATI in atoms [41] and molecules [40]. The focus of our study is on diatomic and triatomic molecular systems, although the extension to more complex systems appears to be straightforward. First, we have validated our formalism comparing the atomic HHG spectra with results extracted from the 3D-TDSE and using a large set of laser intensities and wavelengths. For the molecular systems we have shown our approach is able to capture the interference features, ubiquitously present in every molecular HHG process. As was already described, the core of our model are the saddle-point approximation and the linear combination of atomic orbitals. Thus, the main advantages can be summarized as follows:

(i) The possibility to disentangle the underlying contributions to the HHG spectra. In this way, we could isolate *local* and *cross* processes and also treat both fixed and randomly oriented molecules.

(ii) The low computational cost. By considering our approach involves only 1D and 2D time integrations, all the other quantities being analytical, it is clear that we compute molecular HHG spectra without too much computational effort.

(iii) The concrete feasibility to model complex molecular ground states. For all the studied molecular cases we were able to model reasonably well the initial molecular ground state, varying the parameters of our nonlocal SR potential.

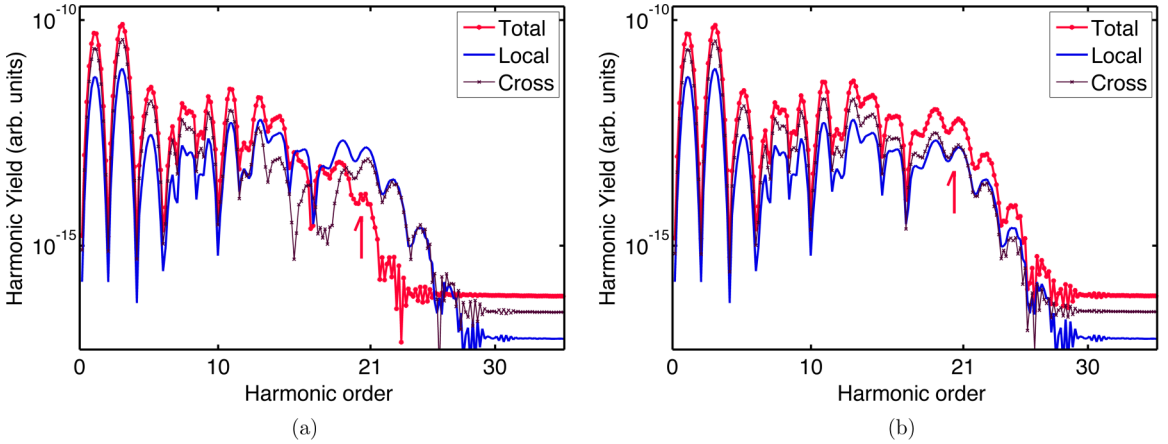

FIG. 11. Different contributions to the H_2O molecular HHG spectra. (a) $\theta = 0°$; (b) $\theta = 90°$.

ACKNOWLEDGMENTS

This work was supported by the project ELI–Extreme Light Infrastructure–phase 2 (Grant No. CZ.02.1.01/0.0/0.0/15_008/0000162) from European Regional Development Fund, Ministerio de Economía y Competitividad through Plan Nacional (Grant No. FIS2016-79508-P, FISICATEAMO, Grant No. FIS2011-30465-C02-01, FrOntiers of QUantum Sciences (FOQUS): Atoms, Molecules, Photons and Quantum Information Grants No. FIS2013-46768-P, No. FIS2014-56774-R, and Severo Ochoa Excellence Grant No. SEV-2015-0522), and funding from the European Unions Horizon 2020 research and innovation Programme under the Marie Sklodowska-Curie Grant Agreement No. 641272 and Laserlab-Europe (Grant No. EU-H2020 654148), Fundació Privada Cellex, and Generalitat de Catalunya (Grant No. SGR 874 and CERCA Programme). N.S. was supported by the Erasmus Mundus Doctorate Program Europhotonics (Grant No. 159224-1-2009-1-FR-ERA MUNDUS-EMJD). N.S., A.C., and M.L. acknowledge ERC AdG OSYRIS, EU FETPRO QUIC and National Science Centre Poland–Symfonia Grant No. 2016/20/W/ST4/00314. J.B. acknowledges Grant No. FIS2014-51478-ERC and the National Science Centre, Poland–Symfonia Grant No. 2016/20/W/ST4/00314. J.A.P.-H. acknowledges support from Laserlab Europe (Grant No. EU-H2020 654148) and the Spanish Ministerio de Economía y Competitividad (FURIAM Project No. FIS2013-47741-R and PALMA Project No. FIS2016-81056-R).

APPENDIX: STRONG-FIELD APPROXIMATION FOR THREE-CENTER MOLECULAR SYSTEMS

In this section, we develop an analytical model to obtain the direct probability transition amplitude, as well as the bound and scattering states, necessary to calculate the HHG spectra for three-center molecular systems. This approach can be considered an extension of the atomic and diatomic models presented in Refs. [40,41]. Our quasiclassical formalism takes advantage of both the SAE and dipole approximations. In addition, we consider the nuclei of the molecule are fixed in space (the so-called frozen-core approximation).

1. Direct transition probability amplitude

We consider a molecular system of three independent atoms, as is shown in Fig. 12, under the influence of an intense and short laser field. In the limit when the wavelength of the laser λ_0 is larger compared with the Bohr radius $a_0 = 0.0529$ nm, the electric field of the laser beam around the interaction region can be considered as spatially homogeneous. This means that the interacting atoms do not experience any spatial dependence of this driving field. Then, only its time variation is taken into account (the above statements define the so-called dipole approximation).

Therefore, the laser electric field can be written as

$$\mathbf{E}(t) = \mathcal{E}_0\, f(t) \sin(\omega_0\, t + \phi_0)\, \mathbf{e}_z. \tag{A1}$$

The field has a carrier frequency $\omega_0 = \frac{2\pi c}{\lambda_0}$, where c is the speed of light, $\mathcal{E}_0$ the laser electric field peak amplitude, and

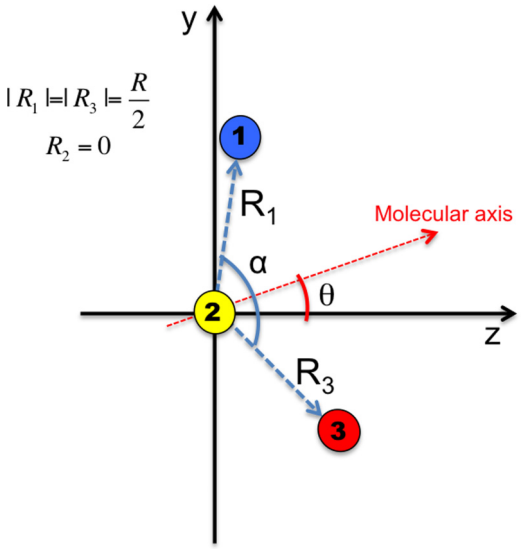

FIG. 12. Three-center molecular system aligned a θ angle with respect to the laser electric field polarization. The red line represents the molecular axis that forms an angle of $\alpha/2$ between $\mathbf{R}_1 = [0, \frac{R}{2}\sin(\frac{\alpha}{2}+\theta), \frac{R}{2}\cos(\frac{\alpha}{2}+\theta)]$ and $\mathbf{R}_3 = [0, -\frac{R}{2}\sin(\frac{\alpha}{2}-\theta), \frac{R}{2}\cos(\frac{\alpha}{2}-\theta)]$.

we consider the laser field is linearly polarized along the z direction. In Eq. (A1), $f(t)$ denotes the envelope of the laser pulse and ϕ_0 defines the CEP (see Sec. III for more details).

The TDSE that describes the whole laser-molecule interaction can be written as

$$\begin{aligned} i\frac{\partial}{\partial t}|\Psi(t)\rangle &= \hat{H}|\Psi(t)\rangle \\ &= [\hat{H}_0 + \hat{V}_{int}(\mathbf{r},t)]|\Psi(t)\rangle, \end{aligned} \tag{A2}$$

where $\hat{H}_0 = \frac{\hat{\mathbf{p}}^2}{2} + \hat{V}(\mathbf{r})$ defines the laser-field free Hamiltonian, with $\hat{\mathbf{p}} = -i\nabla$ the canonical momentum operator and $\hat{V}(\mathbf{r})$ the potential operator that describes the interaction of the nuclei with the active electron. $\hat{V}_{int}(\mathbf{r},t) = -q_e\hat{\mathbf{E}}(t)\cdot\hat{\mathbf{r}}$ represents the interaction of the molecular system with the laser radiation, written in the dipole approximation and length gauge. q_e denotes the electron charge (in atomic units $q_e = -1.0$ a.u.).

We shall restrict our model to the low ionization regime, where the SFA is valid [13,14,49–52]. Therefore, we work in the tunneling regime, where the Keldysh parameter $\gamma = \sqrt{I_p/2U_p}$ (I_p is the ionization potential of the system and $U_p = \frac{\mathcal{E}_0^2}{4\omega_0^2}$ the ponderomotive energy acquired by the electron during its incursion in the laser field) is less than one, i.e., $\gamma < 1$. In addition, we assume that $V(\mathbf{r})$ does not play an important role in the electron dynamics once the electron appears in the continuum.

These observations, and the following three statements, define the standard SFA, namely, the following:

(i) Only the ground $|0\rangle$ and the continuum states $|\mathbf{v}\rangle$ are taken into account in the interaction process.

(ii) There is no depletion of the ground state ($U_p < U_{\text{sat}}$).

(iii) The continuum states are approximated by Volkov states; in the continuum the electron is considered as a free particle solely moving driven by the laser electric field.

For a more detailed discussion of the validity of the above statements, see e.g. Refs. [13,14,41].

Based on (i), we propose a state $|\Psi(t)\rangle = \sum_{j=1}^{3} |\Psi_j(t)\rangle$ to describe the time evolution of the three-center system, i.e., a superposition of three atomic states. In turn, each independent state $|\Psi_j(t)\rangle$ is a coherent superposition of ground $|0\rangle = \sum_{j=1}^{3} |0_j\rangle$ and continuum states $|\mathbf{v}\rangle$ [13,14], i.e.,

$$|\Psi_j(t)\rangle = e^{iI_p t}\left[a(t)|0_j\rangle + \int d^3\mathbf{v}\, b_j(\mathbf{v},t)|\mathbf{v}\rangle\right], \tag{A3}$$

where the subscript $j = 1,2,3$ refers to the position $\mathbf{R}_1$, $\mathbf{R}_2$, and $\mathbf{R}_3$ of each of the atoms in the three-center molecule, respectively.

The factor $a(t)$ represents the amplitude of the ground state and is considered constant in time, i.e., $a(t) \approx 1$: this assumption considers there is no depletion of the ground state and it follows directly from statement (ii). The prefactor $e^{iI_p t}$ represents the phase oscillations that describe the accumulated electron energy in the ground state ($I_p = -E_0$ is the ionization potential of the molecular target, with E_0 the ground-state energy of the three-center molecular system). Furthermore, the transition amplitudes to the continuum states are denoted by $b_j(\mathbf{v},t)$, with $j = 1,2,3$, depending on the atomic nuclei. These amplitudes depend both on the kinetic momentum of the outgoing electron and the laser pulse. Therefore, our main task is to derive a general expression for each transition amplitude $b_j(\mathbf{v},t)$. In order to do so, we substitute Eq. (A3) in (A2). We shall consider that $\hat{H}_0|0_{1,2,3}\rangle = -I_p|0_{1,2,3}\rangle$ and $\hat{H}_0|\mathbf{v}\rangle = \frac{\mathbf{v}^2}{2}|\mathbf{v}\rangle$ hold for the bound and continuum states, respectively. Consequently, the evolution of the transition amplitude $b_j(\mathbf{v},t)$ becomes

$$\begin{aligned} i\int d^3\mathbf{v}\, \dot{b}_j(\mathbf{v},t)\,|\mathbf{v}\rangle \\ = \int d^3\mathbf{v}\left(\frac{\mathbf{v}^2}{2} + I_p\right) b_j(\mathbf{v},t)|\mathbf{v}\rangle + \mathbf{E}(t)\cdot\mathbf{r}|0_j\rangle \\ + \mathbf{E}(t)\cdot\mathbf{r}\int d^3\mathbf{v}\, b_j(\mathbf{v},t)|\mathbf{v}\rangle. \end{aligned} \tag{A4}$$

Note that we have assumed that the electron-nucleus interaction is neglected once the electron appears at the continuum, i.e., $V(\mathbf{r})|\mathbf{v}\rangle = 0$, which corresponds to the statement (iii). Therefore, by multiplying Eq. (A4) by $\langle\mathbf{v}'|$ and after some algebra, the time variation of the transition amplitude $b_j(\mathbf{v},t)$ reads as

$$\begin{aligned} \dot{b}_j(\mathbf{v},t) = -i\left(\frac{\mathbf{v}^2}{2} + I_p\right) b_j(\mathbf{v},t) - i\,\mathbf{E}(t)\cdot\langle\mathbf{v}|\mathbf{r}|0_j\rangle \\ - i\,\mathbf{E}(t)\cdot\int d^3\mathbf{v}'\, b_j(\mathbf{v}',t)\langle\mathbf{v}|\mathbf{r}|\mathbf{v}'\rangle. \end{aligned} \tag{A5}$$

The first term on the right-hand of Eq. (A5) represents the phase evolution of the electron in the oscillating laser electric field. In the second term we have defined the bound-continuum matrix element as

$$-\langle\mathbf{v}|\mathbf{r}|0_j\rangle = \mathbf{d}_j(\mathbf{v}). \tag{A6}$$

The state $|\mathbf{v}\rangle$ represents a scattering state constructed as a plane wave $|\mathbf{v}_p\rangle$ plus corrections on each center position $|\delta\mathbf{v}_j\rangle$.

Based on statement (iii), our formulation only considers the continuum state as a plane wave $|\mathbf{v}_p\rangle$ for the calculation of the bound-continuum matrix element. We shall pay special attention to the computation of Eq. (A6). Notice that the plane waves are not orthogonal to the bound states due to the fact that the latter are defined depending on the relative position of each of the atoms $\mathbf{R}_j$ with respect to the origin of coordinates (see [40] for more details). So, for the $\mathbf{R}_j$ contribution we introduce a correction to the bound-continuum matrix element as

$$\mathbf{d}_j(\mathbf{v}) = -\langle\mathbf{v}_p|\mathbf{r} - \mathbf{R}_j|0_j\rangle = -\langle\mathbf{v}_p|\mathbf{r}|0_j\rangle + \mathbf{R}_j\langle\mathbf{v}_p|0_j\rangle. \tag{A7}$$

The third term of Eq. (A5) defines the continuum-continuum matrix element. In our case, we are interested in describing processes where the electron is ionized and goes to the continuum, never returning to the vicinity of the remaining ion core, i.e., the so-called direct processes. As the direct ionization process should have a larger probability compared with the continuum-continuum one [13,41], one might neglect the rescattering factor $g_m(\mathbf{v},\mathbf{v}') \approx 0$ in the last term of Eq. (A5) [notice that $\langle\mathbf{v}|\mathbf{r}|\mathbf{v}'\rangle = i\nabla_{\mathbf{v}}\delta(\mathbf{v}-\mathbf{v}') - i\mathbf{R}_j\delta(\mathbf{v}-\mathbf{v}') + g_m(\mathbf{v},\mathbf{v}')$].

This is what we refer as zeroth-order solution:

$$\begin{aligned} \partial_t b_{0,j}(\mathbf{v},t) = -i\left[\frac{\mathbf{v}^2}{2} + I_p - \mathbf{R}_j\cdot\mathbf{E}(t)\right] b_{0,j}(\mathbf{v},t) \\ + i\,\mathbf{E}(t)\cdot\mathbf{d}_j(\mathbf{v}). \end{aligned} \tag{A8}$$

The latter equation is easily solved by conventional integration methods (see, e.g., [53]) and considering the Keldysh transformation [49,54]. Therefore, the solution can be written as

$$b_{0,j}(\mathbf{p},t) = i\int_0^t dt'\,\mathbf{E}(t')\cdot\mathbf{d}_j[\mathbf{p} + \mathbf{A}(t')]\exp[-iS_j(\mathbf{p},t,t')]. \tag{A9}$$

Notice that $j = 1,2,3$ represents either an atom located at $\mathbf{R}_1$, $\mathbf{R}_2$, or $\mathbf{R}_3$, respectively. For instance, to obtain the transition amplitude for the atom placed at $\mathbf{R}_1$ we need to set $j = 1$ in Eq. (A9). Additionally, Eq. (A9) is written in terms of the canonical momentum $\mathbf{p} = \mathbf{v} - \mathbf{A}(t)$ [14]. Here, we have considered that the electron appears in the continuum with kinetic momentum $\mathbf{v}(t') = \mathbf{v} - \mathbf{A}(t) + \mathbf{A}(t')$ at the time t', where $\mathbf{v}$ is the final kinetic momentum (note that in atomic units $\mathbf{p} = \mathbf{v}$), and $\mathbf{A}(t) = -\int^t \mathbf{E}(t')dt'$ is the associated vector potential.

Equation (A9) has a direct physical interpretation: it can be understood as the sum of all the ionization events that occur from the time t' to t. Then, the instantaneous transition probability amplitude of an electron at a time t', at which it appears into the continuum with momentum $\mathbf{v}(t') = \mathbf{p} + \mathbf{A}(t')$, is defined by the argument of the $[0,t]$ integral in Eq. (A9). Furthermore, the argument of the exponential phase factor $S_j(\mathbf{p},t,t')$ in Eq. (A9) denotes the "semiclassical action", that defines a possible electron trajectory from the *birth* time t', at position $\mathbf{R}_j$, until the *recombination* one t as

$$S_j(\mathbf{p},t,t') = \int_{t'}^{t} d\tilde{t}\{[\mathbf{p} + \mathbf{A}(\tilde{t})]^2/2 + I_p - \mathbf{R}_j\cdot\mathbf{E}(\tilde{t})\}. \tag{A10}$$

Note that the transition amplitude equations obtained so far depend on the position from which the electron is tunnel ionized to the continuum. The semiclassical action $S_j(\mathbf{p},t,t')$ contains this dependency as well.

Considering we are interested in obtaining the transition amplitude $b_{0,j}(\mathbf{p},t)$ at the end of the laser pulse, the time t is set at $t = t_F$. Consequently, we shall define the integration time window as $t \in [0,t_F]$. Furthermore, we set $\mathbf{E}(0) = \mathbf{E}(t_F) = \mathbf{0}$, in such a way to make sure that the laser electric field is a time oscillating wave and does not contain static components [the same arguments apply to the vector potential $\mathbf{A}(t)$]. Finally, the total transition amplitude for the direct process taking place in our three-center molecular system reads as

$$b_0(\mathbf{p},t) = \sum_{j=1}^{3} b_{0,j}(\mathbf{p},t). \tag{A11}$$

2. Bound-states calculation

In this section, we are going to develop analytical expressions to obtain the bound states for our three-center molecular system. As in the atomic and diatomic cases we have chosen a nonlocal SR potential to describe the interaction of the electrons with the nuclei. We consider a molecular system with three fixed nuclei under the SAE approximation. Our purpose is to find the analytical dependency of the bound-state wave functions, that allow us to compute the bound-continuum matrix element and the direct transition amplitudes (A11).

The Hamiltonian for the molecular system in the momentum representation can be written in a similar way as for the diatomic case, i.e.,

$$\hat{H}_{\mathbf{M}}(\mathbf{p},\mathbf{p}') = \frac{\hat{p}^2}{2}\delta(\mathbf{p}-\mathbf{p}') + \hat{V}_{\mathbf{M}}(\mathbf{p},\mathbf{p}'), \tag{A12}$$

where the first term on the right-hand side is the kinetic energy operator and the second one describes the interacting nonlocal SR potential between the active electron and each molecular nuclei:

$$\hat{V}_{\mathbf{M}}(\mathbf{p},\mathbf{p}') = -\gamma'\,\phi(\mathbf{p})\,\phi(\mathbf{p}')\sum_{j=1}^{3} e^{-i\mathbf{R}_j\cdot(\mathbf{p}-\mathbf{p}')}, \tag{A13}$$

where $\phi(\mathbf{p}) = \frac{1}{\sqrt{\mathbf{p}^2+\Gamma^2}}$ is an auxiliary function and $\gamma' = \frac{\gamma}{3}$ is a parameter related with the shape of the ground state. By using $\hat{H}_{\mathbf{M}}(\mathbf{p},\mathbf{p}')$ from Eq. (A12), we write the stationary Schrödinger equation as follows:

$$\hat{H}_{\mathbf{M}}(\mathbf{p})\Psi(\mathbf{p}) = \int d^3\mathbf{p}'\,\hat{H}_{\mathbf{M}}(\mathbf{p},\mathbf{p}')\Psi(\mathbf{p}') = E_0\,\Psi(\mathbf{p}), \tag{A14}$$

where E_0 denotes the energy of the bound state. Thus, for our three-center system the Schrödinger equation reads as

$$\left(\frac{p^2}{2}+I_p\right)\Psi_{0\mathbf{M}}(\mathbf{p}) = \gamma'\,\phi(\mathbf{p})\sum_{j=1}^{3} e^{-i\mathbf{R}_j\cdot\mathbf{p}} \times \int d^3\mathbf{p}'\Psi_{0\mathbf{M}}(\mathbf{p}')\phi(\mathbf{p}')e^{i\mathbf{R}_j\cdot\mathbf{p}'}. \tag{A15}$$

Defining new variables $\breve{\varphi}_j$ as

$$\breve{\varphi}_j = \int d^3\mathbf{p}'\Psi_{0\mathbf{M}}(\mathbf{p}')\phi(\mathbf{p}')e^{i\mathbf{R}_j\cdot\mathbf{p}'} = \int \frac{d^3\mathbf{p}'\Psi_{0\mathbf{M}}(\mathbf{p}')e^{i\mathbf{R}_j\cdot\mathbf{p}'}}{\sqrt{p'^2+\Gamma^2}}, \tag{A16}$$

we could analytically obtain the bound states by solving Eq. (A15) in the momentum representation. Explicitly, we can write

$$\left(\frac{p^2}{2}+I_p\right)\Psi_{0\mathbf{M}}(\mathbf{p}) = \gamma'\,\phi(\mathbf{p})\sum_{j=1}^{3} e^{-i\mathbf{R}_j\cdot\mathbf{p}}\,\breve{\varphi}_j, \tag{A17}$$

where I_p denotes the ionization potential that is related to the ground-state potential energy by $E_0 = -I_p$. The wave function $\Psi_{0\mathbf{M}}(\mathbf{p})$ for the bound state in momentum space is defined as

$$\Psi_{0\mathbf{M}}(\mathbf{p}) = \frac{\gamma'}{\sqrt{(p^2+\Gamma^2)}\left(\frac{p^2}{2}+I_p\right)}\sum_{j=1}^{3}\breve{\varphi}_j e^{-i\mathbf{R}_j\cdot\mathbf{p}}. \tag{A18}$$

In order to find the value of the constants, we multiply and divide Eq. (A18) by $e^{-i\mathbf{R}_j\cdot\mathbf{p}}$ and $\sqrt{p^2+\Gamma^2}$, respectively. After some algebra we find that

$$\begin{aligned}\breve{\varphi}_1 I_1 &= \breve{\varphi}_2 I_2 + \breve{\varphi}_3 I_3,\\ \breve{\varphi}_2 I_1 &= \breve{\varphi}_1 I_2 + \breve{\varphi}_3 I_2,\\ \breve{\varphi}_3 I_1 &= \breve{\varphi}_2 I_2 + \breve{\varphi}_1 I_3,\end{aligned} \tag{A19}$$

where I_1, I_2, and I_3 read as

$$I_1 = 1 - \gamma'\int \frac{d^3\mathbf{p}\,\phi^2(\mathbf{p})}{\left(\frac{p^2}{2}+I_p\right)}, \tag{A20}$$

$$\begin{aligned}I_2 &= \gamma'\int \frac{d^3\mathbf{p}\,\phi^2(\mathbf{p})}{\left(\frac{p^2}{2}+I_p\right)}e^{i(\mathbf{R}_1-\mathbf{R}_2)\cdot\mathbf{p}}\\ &= \gamma'\int \frac{d^3\mathbf{p}\,\phi^2(\mathbf{p})}{\left(\frac{p^2}{2}+I_p\right)}e^{i(\mathbf{R}_3-\mathbf{R}_2)\cdot\mathbf{p}}\end{aligned} \tag{A21}$$

and

$$\begin{aligned}I_3 &= \gamma'\int \frac{d^3\mathbf{p}\,\phi^2(\mathbf{p})}{\left(\frac{p^2}{2}+I_p\right)}e^{i(\mathbf{R}_1-\mathbf{R}_3)\cdot\mathbf{p}}\\ &= \gamma'\int \frac{d^3\mathbf{p}\,\phi^2(\mathbf{p})}{\left(\frac{p^2}{2}+I_p\right)}e^{-i(\mathbf{R}_1-\mathbf{R}_3)\cdot\mathbf{p}},\end{aligned} \tag{A22}$$

respectively.

Solving the system of equations (A19) we find the relations between the $\breve{\varphi}_j$ defined by Eqs. (A16) and I_1, I_2, and I_3. Here, Eq. (A19) is solved with the restriction

$$I_3 = \frac{I_1^2 - 2\,I_2^2}{I_1}; \quad I_1 \neq 0, \tag{A23}$$

and

$$\breve{\varphi}_1 = \breve{\varphi}_3 = \frac{I_2}{I_1 - I_3}\,\breve{\varphi}_2. \tag{A24}$$

I_1, I_2, and I_3 can be written in spherical coordinates as

$$I_1 = 1 - \frac{4\pi^2\gamma'}{\Gamma + \sqrt{2I_p}}, \tag{A25}$$

$$I_2 = \frac{8\pi^2\gamma'}{R}\left\{\frac{e^{-\frac{R\Gamma}{2}} - e^{-\frac{R\sqrt{2I_p}}{2}}}{2I_p - \Gamma^2}\right\}, \tag{A26}$$

and

$$I_3 = \frac{4\pi^2\gamma'}{R\,\sin(\alpha/2)}\left\{\frac{e^{-R\sin(\alpha/2)\Gamma} - e^{-R\sin(\alpha/2)\sqrt{2I_p}}}{2I_p - \Gamma^2}\right\}. \tag{A27}$$

Finally, Eq. (A18) reads as

$$\Psi_{0\mathbf{M}}(\mathbf{p}) = \frac{\mathcal{M}_{3\mathrm{N}}}{\sqrt{(p^2+\Gamma^2)}\left(\frac{p^2}{2}+I_p\right)}\left[\left(\frac{I_2}{I_1 - I_3}\right)e^{-i\mathbf{R}_1\cdot\mathbf{p}} + e^{-i\mathbf{R}_2\cdot\mathbf{p}} + \left(\frac{I_2}{I_1 - I_3}\right)e^{-i\mathbf{R}_3\cdot\mathbf{p}}\right], \tag{A28}$$

where $\mathcal{M}_{3\mathrm{N}} = \gamma'\,\breve{\varphi}_1 = \frac{\gamma}{3}\,\breve{\varphi}_1$ is a normalization constant. It can be calculated using the usual normalization condition

$$\int d^3\mathbf{p}\,\Psi_{0\mathbf{M}}(\mathbf{p})^*\,\Psi_{0\mathbf{M}}(\mathbf{p}) = 1. \tag{A29}$$

From the above equation $\mathcal{M}_{3\mathrm{N}}$ can be written as

$$1 = {\mathcal{M}_{3\mathrm{N}}}^2\,I_4, \tag{A30}$$

with I_4 defined as

$$\begin{aligned} I_4 = \left(\frac{2\,I_2}{I_1 - I_3}\right)^2 &\left\{\frac{4\pi^2}{R(2I_p-\Gamma^2)^2}\left[e^{-R\Gamma} - e^{-R\sqrt{2I_p}}\left(\frac{2\sqrt{2I_p} + R(2I_p-\Gamma^2)}{2\sqrt{2I_p}}\right)\right]\right. \\ &\left. + \frac{4\pi^2}{R\cos(\alpha/2)(2I_p-\Gamma^2)^2}\left[e^{-R\cos(\alpha/2)\Gamma} - e^{-R\cos(\alpha/2)\sqrt{2I_p}}\left(\frac{2\sqrt{2I_p} + R\cos(\alpha/2)(2I_p-\Gamma^2)}{2\sqrt{2I_p}}\right)\right]\right\} \\ &+ \frac{8\,I_2^2}{I_1 - I_3}\frac{4\pi^2}{\frac{R}{2}(2I_p-\Gamma^2)^2}\left[e^{-\frac{R}{2}\Gamma} - e^{-\frac{R}{2}\sqrt{2I_p}}\left(\frac{2\sqrt{2I_p} + \frac{R}{2}(2I_p-\Gamma^2)}{2\sqrt{2I_p}}\right)\right] + \frac{4\pi^2(\sqrt{2I_p}-\Gamma)^2}{\sqrt{2I_p}(2I_p-\Gamma^2)^2}. \end{aligned} \tag{A31}$$

With the exact knowledge of $\mathcal{M}_{3N}$ we have now defined the bound state in our three-center molecular system from Eq. (A28). Notice that the dependency of the system energy with the internuclear distance appears from the solution of the system of equations (A19).

3. Bound-continuum matrix element

The total bound-continuum matrix element for the three-center molecular system is defined as a sum:

$$\mathbf{d}_{3\mathrm{N}}(\mathbf{v}) = -\sum_{j=1}^{3}(\langle\mathbf{v}_p|\mathbf{r}|0_j\rangle + \mathbf{R}_j\langle\mathbf{v}_p|0_j\rangle). \tag{A32}$$

Equation (A32) can be explicitly written as

$$\mathbf{d}_{3\mathrm{N}}(\mathbf{p}_0) = -2i\,\mathcal{M}_{3\mathrm{N}}\mathcal{A}(\mathbf{p}_0)\left[\frac{I_2}{I_1 - I_3}\,(e^{-i\mathbf{R}_1\cdot\mathbf{p}_0} + e^{-i\mathbf{R}_3\cdot\mathbf{p}_0}) + 1\right], \tag{A33}$$

where

$$\mathcal{A}(\mathbf{p}_0) = \boldsymbol{\nabla}_{\mathbf{p}}\left[\frac{1}{(p^2+\Gamma^2)^{\frac{1}{2}}(p^2+2I_p)}\right]\Big|_{\mathbf{p}_0} = -\mathbf{p}_0\,\frac{\left(3p_0^2 + 2I_p + 2\Gamma^2\right)}{\left(p_0^2+\Gamma^2\right)^{\frac{3}{2}}\left(p_0^2+2I_p\right)^2}. \tag{A34}$$

Finally, notice that we could extract the contributions of each center from Eq. (A33), i.e.,

$$\mathbf{d}_1(\mathbf{p}_0) = -2i\,\mathcal{M}_{3\mathrm{N}}\mathcal{A}(\mathbf{p}_0)\left(\frac{I_2}{I_1 - I_3}\right)e^{-i\mathbf{R}_1\cdot\mathbf{p}_0}, \tag{A35}$$

$$\mathbf{d}_2(\mathbf{p}_0) = -2i\,\mathcal{M}_{3\mathrm{N}}\mathcal{A}(\mathbf{p}_0), \tag{A36}$$

and

$$\mathbf{d}_3(\mathbf{p}_0) = -2i\,\mathcal{M}_{3N}\mathcal{A}(\mathbf{p}_0)\left(\frac{I_2}{I_1 - I_3}\right)e^{-i\mathbf{R}_3\cdot\mathbf{p}_0}. \tag{A37}$$

[1] A. L'Huillier, K. J. Schafer, and K. C. Kulander, Theoretical aspects of intense field harmonic generation, J. Phys. B: At., Mol. Opt. Phys. **24**, 3315 (1991).

[2] C. Lyngå, A. L'Huillier, and C.-G. Wahlström, High-order harmonic generation in molecular gases, J. Phys. B: At., Mol. Opt. Phys. **29**, 3293 (1996).

[3] F. Krausz and M. Ivanov, Attosecond physics, Rev. Mod. Phys. **81**, 163 (2009).

[4] S. Ghimire, A. D. DiChiara, E. Sistrunk, P. Agostini, L. F. DiMauro, and D. A. Reis, Observation of high-order harmonic generation in a bulk crystal, Nat. Phys. **7**, 138 (2011).

[5] G. Vampa, C. R. McDonald, G. Orlando, D. D. Klug, P. B. Corkum, and T. Brabec, Theoretical Analysis of High-Harmonic Generation in Solids, Phys. Rev. Lett. **113**, 073901 (2014).

[6] M. F. Ciappina, J. A. Pérez-Hernández, A. S. Landsman, W. Okell, S. Zherebtsov, B. Förg, J. Schötz, L. Seiffert, T. Fennel, T. Shaaran, T. Zimmermann, A. Chacón, R. Guichard, A. Zaïr, J. W. G. Tisch, J. P. Marangos, T. Witting, A. Braun, S. A. Maier, L. Roso, M. Krüger, P. Hommelhoff, M. F. Kling, F. Krausz, and M. Lewenstein, Attosecond physics at the nanoscale, Rep. Prog. Phys. (2017), doi: 10.1088/1361-6633/aa574e.

[7] P. B. Corkum and F. Krausz, Attosecond science, Nat. Phys. **3**, 381 (2007).

[8] M. Lein, Molecular imaging using recolliding electrons, J. Phys. B: At., Mol. Opt. Phys. **40**, R135 (2007).

[9] M. Lein, N. Hay, R. Velotta, J. P. Marangos, and P. L. Knight, Interference effects in high-order harmonic generation with molecules, Phys. Rev. A **66**, 023805 (2002).

[10] T. Kanai, S. Minemoto, and H. Sakai, Quantum interference during high-order harmonic generation from aligned molecules, Nature (London) **435**, 470 (2005).

[11] R. Torres, N. Kajumba, J. G. Underwood, J. S. Robinson, S. Baker, J.W. G. Tisch, R. de Nalda, W. A. Bryan, R. Velotta, C. Altucci, I. C. E. Turcu, and J. P. Marangos, Probing Orbital Structure of Polyatomic Molecules by High-Order Harmonic Generation, Phys. Rev. Lett. **98**, 203007 (2007).

[12] T. Morishita, A. T. Le, Z. Chen, and C. D. Lin, Accurate Retrieval of Structural Information from Laser-Induced Photoelectron and High-Order Harmonic Spectra by Few-Cycle Laser Pulses, Phys. Rev. Lett. **100**, 013903 (2008).

[13] M. Lewenstein, K. C. Kulander, K. J. Schafer, and P. H. Bucksbaum, Rings in above-threshold ionization: A quasiclassical analysis, Phys. Rev. A **51**, 1495 (1995).

[14] M. Lewenstein, Ph. Balcou, M. Y. Ivanov, A. L'Huillier, and P. B. Corkum, Theory of high-harmonic generation by low-frequency laser fields, Phys. Rev. A **49**, 2117 (1994).

[15] P. B. Corkum, Plasma Perspective on Strong Field Multiphoton Ionization, Phys. Rev. Lett. **71**, 1994 (1993).

[16] C. Cornaggia, M. Schmidt, and D. Normand, Coulomb explosion of CO_2 in an intense femtosecond laser field, J. Phys. B: At., Mol. Opt. Phys. **27**, L123 (1994).

[17] M. Schmidt, D. Normand, and C. Cornaggia, Laser-induced trapping of chlorine molecules with pico- and femtosecond pulses, Phys. Rev. A **50**, 5037 (1994).

[18] D. G. Lappas and J. P. Marangos, Orientation dependence of high-order harmonic generation in hydrogen molecular ions, J. Phys. B: At., Mol. Opt. Phys. **33**, 4679 (2000).

[19] R. Velotta, N. Hay, M. B. Mason, M. Castillejo, and J. P. Marangos, High-Order Harmonic Generation in Aligned Molecules, Phys. Rev. Lett. **87**, 183901 (2001).

[20] N. Hay, R. Velotta, M. Lein, R. de Nalda, E. Heesel, M. Castillejo, and J. P. Marangos, High-order harmonic generation in laser-aligned molecules, Phys. Rev. A **65**, 053805 (2002).

[21] M. Lein, N. Hay, R. Velotta, J. P. Marangos, and P. L. Knight, Role of the Intramolecular Phase in High-Harmonic Generation, Phys. Rev. Lett. **88**, 183903 (2002).

[22] M. Yu. Ivanov and P. B. Corkum, Generation of high-order harmonics from inertially confined molecular ions, Phys. Rev. A **48**, 580 (1993).

[23] T. Zuo, S. Chelkowski, and A. D. Bandrauk, Harmonic generation by the H_2^+ molecular ion in intense laser fields, Phys. Rev. A **48**, 3837 (1993).

[24] H. Yu and A. D. Bandrauk, Three-dimensional Cartesian finite element method for the time dependent Schrödinger equation of molecules in laser fields, J. Chem. Phys. **102**, 1257 (1995).

[25] P. Moreno, L. Plaja, and L. Roso, Ultrahigh harmonic generation from diatomic molecular ions in highly excited vibrational states, Phys. Rev. A **55**, R1593 (1997).

[26] R. Kopold, W. Becker, and M. Kleber, Model calculations of high-harmonic generation in molecular ions, Phys. Rev. A **58**, 4022 (1998).

[27] O. E. Alon, V. Averbukh, and N. Moiseyev, Selection Rules for the High Harmonic Generation Spectra, Phys. Rev. Lett. **80**, 3743 (1998).

[28] V. Averbukh, O. E. Alon, and N. Moiseyev, High-order harmonic generation by molecules of discrete rotational symmetry interacting with circularly polarized laser field, Phys. Rev. A **64**, 033411 (2001).

[29] A. D. Bandrauk and H. Yu, High-order harmonic generation by one- and two-electron molecular ions with intense laser pulses, Phys. Rev. A **59**, 539 (1999).

[30] T. Kreibich, M. Lein, V. Engel, and E. K. U. Gross, Even-Harmonic Generation due to Beyond-Born-Oppenheimer Dynamics, Phys. Rev. Lett. **87**, 103901 (2001).

[31] M. Lein, P. P. Corso, J. P. Marangos, and P. L. Knight, Orientation dependence of high-order harmonic generation in molecules, Phys. Rev. A **67**, 023819 (2003).

[32] M. F. Ciappina, C. C. Chirilă, and M. Lein, Influence of Coulomb continuum wave functions in the description of high-order harmonic generation with H_2^+, Phys. Rev. A **75**, 043405 (2007).

[33] J. Itatani, J. Levesque, D. Zeidler, H. Niikura, H. Pépin, J. C. Kieffer, P. B. Corkum, and D. M. Villeneuve, Tomographic imaging of molecular orbitals, Nature (London) **432**, 867 (2004).

[34] M. F. Ciappina, A. Becker, and A. Jaroń-Becker, Multislit interference patterns in high-order harmonic generation in C_{60}, Phys. Rev. A **76**, 063406 (2007).

[35] M. F. Ciappina, A. Becker, and A. Jaroń-Becker, High-order harmonic generation in fullerenes with icosahedral symmetry, Phys. Rev. A **78**, 063405 (2008).

[36] T. Laarmann, I. Shchatsinin, A. Stalmashonak, M. Boyle, N. Zhavoronkov, J. Handt, R. Schmidt, C.P. Schulz, and I. V. Hertel, Control of Giant Breathing Motion in C_{60} with Temporally Shaped Laser Pulses, Phys. Rev. Lett. **98**, 058302 (2007).

[37] O. Smirnova, Y. Mairesse, S. Patchkovskii, N. Dudovich, D. M. Villeneuve, P. Corkum, and M. Y. Ivanov, High harmonic interferometry of multi-electron dynamics in molecules, Nature (London) **460**, 972 (2009).

[38] S. Haessler, J. Caillat, W. Boutu, C. Giovanetti-Teixeira, T. Ruchon, T. Auguste, Z. Diveki, P. Breger, B. Carré, R. Taïeb, and P. Salières, Attosecond imaging of molecular electronic wavepackets, Nat. Phys. **6**, 200 (2010).

[39] P. M. Kraus, B. Mignolet, D. Baykusheva, A. Rupenyan, L. Horný, E. F. Penka, G. Grassi, O. I. Tolstikhin, J. Schneider, F. Jensen, L. B. Madsen, A. D. Bandrauk, F. Remacle, and H. J. Wörner, Measurement and laser control of attosecond charge migration in ionized iodoacetylene, Science **350**, 790 (2015).

[40] N. Suárez, A. Chacón, M. F. Ciappina, B. Wolter, J. Biegert, and M. Lewenstein, Above-threshold ionization and laser-induced electron diffraction in diatomic molecules, Phys. Rev. A **94**, 043423 (2016).

[41] N. Suárez, A. Chacón, M. F. Ciappina, J. Biegert, and M. Lewenstein, Above-threshold ionization and photoelectron spectra in atomic systems driven by strong laser fields, Phys. Rev. A **92**, 063421 (2015).

[42] H. Hetzheim, C. Figueira de Morisson Faria, and W. Becker, Interference effects in above-threshold ionization from diatomic molecules: Determining the internuclear separation, Phys. Rev. A **76**, 023418 (2007).

[43] C. C. Chirilă and M. Lein, Strong-field approximation for harmonic generation in diatomic molecules, Phys. Rev. A **73**, 023410 (2006).

[44] M. Busuladžić, A. Gazibegović-Busuladžić, D. B. Milošević, and W. Becker, Angle-Resolved High-Order above-Threshold Ionization of a Molecule: Sensitive tool for Molecular Characterization, Phys. Rev. Lett **100**, 203003 (2008).

[45] C. C. Chirilă, I. Dreissigacker, E. V. van der Zwan, and M. Lein, Emission times in high-order harmonic generation, Phys. Rev. A **81**, 033412 (2010).

[46] D. Gabor, Theory of communication. Part 1: The analysis of information, J. Inst. Electr. Eng. **93**, 429 (1946).

[47] Nist standard reference data program, http://webbook.nist.gov/cgi/cbook.cgi?ID=124-38-9

[48] Nist standard reference data program, http://webbook.nist.gov/cgi/cbook.cgi?ID=C7732185

[49] L. V. Keldysh, Ionization in the field of a strong electromagnetic wave, Zh. Eksp. Teor. Fiz. **47**, 1945 (1965) [Sov. Phys.–JETP **20**, 1307 (1965)].

[50] F. H. M. Faisal, Multiple absorption of laser photons by atoms, J. Phys. B: At. Mol. Phys. **6**, L89 (1973).

[51] H. R. Reiss, Effect of an intense electromagnetic field on a weakly bound system, Phys. Rev. A **22**, 1786 (1980).

[52] J. Grochmalicki, J. R. Kukliński, and M. Lewenstein, Above-threshold ionisation and electron scattering in intense laser fields, J. Phys. B: At. Mol. Phys. **19**, 3649 (1986).

[53] L. Elsgoltz, *Differential Equations and the Calculus of Variations* (University Press of the Pacific, Miami, 2003).

[54] F. Ehlotzky, Harmonic generation in Keldysh-type models, Nuovo Cimento **14**, 517 (1992).